THIS REPORT HAS BEEN DELIMITED
AND CLEARED FOR PUBLIC RELEASE
UNDER DOD DIRECTIVE 5200.20 AND
NO RESTRICTIONS ARE IMPOSED UPON
ITS USE AND DISCLOSURE.

DISTRIBUTION STATEMENT A

APPROVED FOR PUBLIC RELEASE;
DISTRIBUTION UNLIMITED.

AD-A008 042

STUDIES OF MICROWAVE REMOTE SENSING
OF ATMOSPHERIC PARAMETERS

Norman E. Gaut, et al

Environmental Research and Technology,
Incorporated

Prepared for:

Air Force Cambridge Research Laboratories

August 1974

113107

ADA008042

STUDIES OF MICROWAVE REMOTE SENSING OF ATMOSPHERIC PARAMETERS

Norman E. Gaut
Mary Grace Fowler
Ronald G. Isaacs
David T. Chang
Edward C. Reifenstein, III

Environmental Research & Technology, Inc.
696 Virginia Road
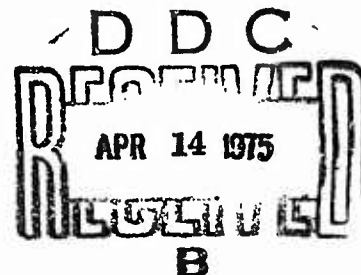Concord, Massachusetts 01742

August 1974

Final Report for Period of March 1973 - June 1974

DDC

APR 14 1975

B

71

Qualified requestors may obtain additional copies from
the Defense Documentation Center.   All others should
apply to the National Technical Information Service.

REPORT DOCUMENTATION PAGE		READ INSTRUCTIONS BEFORE COMPLETING FORM
1. REPORT NUMBER AFCRL-TR-75-0007	2. GOVT ACCESSION NO.	3. RECIPIENT'S CATALOG NUMBER
4. TITLE (and Subtitle) STUDIES OF MICROWAVE REMOTE SENSING OF ATMOSPHERIC PARAMETERS		5. TYPE OF REPORT & PERIOD COVERED Scientific - Final March 1973 - June 1974
		6. PERFORMING ORG. REPORT NUMBER P-512
7. AUTHOR(s) Ronald G. Isaacs Norman E. Gaut David T. Chang Mary Grace Fowler Edward C. Reifenstein, III		8. CONTRACT OR GRANT NUMBER(s) F19628-73-C-0195
9. PERFORMING ORGANIZATION NAME AND ADDRESS Environmental Research & Technology, Inc. 696 Virginia Road Concord, Massachusetts 01742		10. PROGRAM ELEMENT, PROJECT, TASK AREA & WORK UNIT NUMBERS 8682-03-01 62101F
11. CONTROLLING OFFICE NAME AND ADDRESS Air Force Cambridge Research Laboratories Hanscom AFB, Massachusetts 01731 Contract Monitor: Vincent J. Falcone, Jr./LZN		12. REPORT DATE August 1974
		13. NUMBER OF PAGES 71
14. MONITORING AGENCY NAME & ADDRESS(if different from Controlling Office)		15. SECURITY CLASS. (of this report) Unclassified
		15a. DECLASSIFICATION/DOWNGRADING SCHEDULE

16. DISTRIBUTION STATEMENT (of this Report)

Approved for public release; distribution unlimited.

17. DISTRIBUTION STATEMENT (of the abstract entered in Block 20, if different from Report)

Approved for public release; distribution unlimited.

18. SUPPLEMENTARY NOTES

Tech, Other

19. KEY WORDS (Continue on reverse side if necessary and identify by block number)

atmospheric temperature profiles
microwave radiometry
microwave remote sensing

20. ABSTRACT (Continue on reverse side if necessary and identify by block number)

    This is the final report in a study for AFCRL to evaluate the effects of
clouds and precipitation on temperature profiling with microwave systems. As
part of this study several related investigations were made. These included
a comparison of the Gross-Reber and Van Vleck-Weisskopf line shapes for oxygen
absorption which showed that the two models agreed well on the oxygen lines
near 60 GHz and 118 GHz, but that the Van Vleck-Weisskopf model significantly
overestimated the attenuation between 70 GHz and 100 GHz. An approximation of
the effect of precipitation at microwave frequencies was also developed. This

DD FORM 1473 1 JAN 73   EDITION OF 1 NOV 65 IS OBSOLETE

model provided attenuation results in close agreement with those computed using full Mie theory, while avoiding the computational complexities associated with a detailed treatment of scattering effects.

With the Gross-Reber line shape and the precipitation model incorporated in the simulation programs, sets of channels in two 60 GHz oxygen complex and near the 118 GHz oxygen line were selected, simulated, and inverted for atmospheric conditions representing mid latitude spring and tropical summer. The results of the inversions from each set of channels were quite good through the 118 GHZ were slightly less accurate at low altitudes due to a greater sensitivity to water vapor. Separate inversion analyses for specific cloud and hydrometeor conditions showed that the 60 GHz channels were more accurate for temperature profiling in the presence of clouds and that temperature inversion results in the presence of rain were seriously degraded for both sets of channels.

Inversion for temperature data using these channels in the uplooking mode showed excellent results up to 500 mb, without any channel optimization. Separate investigations of the use of these oxygen channels with channels near the 22 GHz and 183 GHz water vapor lines showed great promise in the determination of cloud top height, cloud phase, layered liquid water and prop-size distribution.

ACKNOWLEDGMENTS

TABLE OF CONTENTS

Preceding page blank

LIST OF FIGURES

LIST OF FIGURES (Continued)

viii

LIST OF TABLES

1. INTRODUCTION

1.1 Purpose

On 11 December 1972, the Nimbus 5 satellite was successfully launched into a near circular orbit carrying the five-channel Nimbus E Microwave Spectrometer (NEMS). Since launch, this radiometer system has transmitted a large volume of data from which atmospheric temperature profiles and integrated water vapor values have been successfully inferred. This experiment, the NEMS, has demonstrated conclusively that microwave radiometry is a viable tool to obtain global measurements of atmospheric parameters from orbiting spacecraft on a routine basis.

In recognition of the potentials of such a measurement system to satisfy its needs for global atmospheric data, the U. S. Air Force initiated a program (under Contract No. F047,1-72-C-0227) to define the configuration for a system which can best provide the Air Force with operational data on a global basis, within the constraints of weight and power limitations imposed by the spacecraft used in the Air Force's Defense Meteorological Satellite Program (DMSP). Environmental Research & Technology, Inc. (ERT) contributed to this program by performing analytical studies of the expected performance of a system configuration under a number of geophysical conditions (Gaut, Reifenstein, Chang, and Blinn, 1973). The results of this study demonstrate the usefulness of a microwave system, even within the severe limitations placed on the system design by the spacecraft. It now appears that the Air Force will proceed with the procurement of actual microwave radiometer systems for launch in the 1977 time frame.

The system under consideration by the Air Force is based on the state of the art in component manufacturing techniques and on the current analytical understanding of the interaction between microwave radiation and atmospheric parameters. A number of developments have taken place which suggest that the concepts in microwave remote sensing of atmospheric parameters need to be further analyzed and refined to advance the state of the art in anticipation of future generations of sensors. The purpose of this study is to develop models, analysis techniques, and to perform analyses of a number of special problems in microwave remote probing of atmospheric parameters. The results

are useful in interpreting data expected from the first microwave sensor from the DMSP and in designing future systems.

1.2   Scope

The study addresses itself to two main topics of research and analysis: the effects of clouds and hydrometeors on temperature profiling, and the possibility of obtaining cloud information from microwave remote sensing. However, in the course of achieving these objectives, other developments in ERT's analytical procedures were made. The most significant of these include:

- Implementation of the Gross-Reber line-shape model for the oxygen absorption coefficients

- Extension of analysis of temperature inversion accuracies to the 118 GHz line

- Development of an approximate model for the analysis of the effects of precipitation

- Analysis of the application of the 183 GHz line shape for atmospheric probing

The results of these efforts are organized into three major sections in this report. In Section 2, the precipitation model is discussed. The discussion includes the assumptions and limitations of the model. Computations made using the model are compared with results using the full Mie approach and with results using the Staelin approximation for the analysis of cloud effects.

Detailed studies of the problems associated with temperature inversions are presented in Section 3. The differences in the weighting functions and, therefore, in temperature inversion, are first discussed for selected frequencies. Inversion results using channels in the 60 GHz complex are then compared with results obtained for the 118 GHz line. The effects of clouds and precipitation on temperature sounding in each of the two oxygen absorption regions are shown by actual inversion results using ensembles of data, with and without hydrometeors. Finally, the effects of differing drop size distributions are separately analyzed and presented using the full Mie approach.

2

In Section 4 the results of analysis of remote sensing of clouds by microwave radiometry are presented. Various combinations of channels were analyzed in an attempt to define the parameters which could be inferred. The parameters included liquid cloud top height and ice cloud top height, cloud liquid water profile, and drop size parameters. In these analyses, use was made of the 183 GHz water vapor line.

Many of the problems and techniques examined in this study have never previously been explored in detail. Thus, the results provided in this study are preliminary. Conclusions reached on the basis of these results are summarized in Section 5.

2. PRECIPITATION MODEL

2.1 Background

Precipitation droplets are primary contributors to nonresonant opacity in the microwave region of the spectrum. As a consequence, the presence of rain may severely limit the accuracy of atmospheric temperature profile retrieval from microwave measurements. Evaluation of the effects of precipitation on temperature measurements by "exact" means is at best difficult to perform due to the computational complexities involved. Therefore, the purpose of the work described in this section is the development of an approximation to the interaction which would permit useful analysis of precipitation effects.

The model is basically an analytical extension of an existing approximation model for the analysis of clouds. The development recognizes that the essential difference between precipitating and nonprecipitating clouds is in the nature of their respective drop size distributions. The radiative properties of nonprecipitating clouds may be derived by assuming individual cloud droplets to be Rayleigh scatterers and integrating over the range of cloud droplet sizes. This leads to an analytical form for the cloud extinction coefficient whose properties in the centimeter wavelength region have been evaluated (Staelin, 1966; Gaut and Reifenstein, 1970). Unfortunately, precipitation droplets are one to two orders of magnitude larger than cloud droplets, and the Rayleigh approximation breaks down (Westwater, 1972). A general solution to the problem is available in the form of the Mie (1908) theory solutions. However, the extinction efficiency factor must be computed for each drop size and temperature pair at a given wavelength and then integrated across the distribution of droplet sizes within the ensemble in order to yield the extinction coefficient. This calculation would involve significant expense if implemented within the intricacies of an operational computation scheme. Thus, there is a distinct advantage to employing an approximation.

This section describes a model of the interaction between the radiation field and the precipitation droplets which approximates the extinction due to the presence of both small and large droplets and which does not

require undue amounts of computation time. It should be emphasized that no attempt was made to develop an exact radiative transfer model in which the scattering is treated as a source function. Instead, the model treats scattering as an enhancement in the extinction. The line of reasoning employed has been to extend the present treatment of nonprecipitating clouds to include the effects of large droplets. In this sense it is an analytical extension of the Staelin approximation. The results described provide wavelength, temperature, and precipitation parameter dependencies of the extinction coefficient in a relatively simple analytical form. The dependence of the extinction coefficient on rainfall rate is shown to compare favorably with comparisons based on the full Mie Theory and radar measurements. In addition, comparisons with the Staelin approximation are also presented.

2.2 Theoretical

The unit volume extinction coefficient due to an ensemble of droplets is given by the convolution of the extinction cross section for a droplet of given radius with the drop size distribution function:

$$\gamma_E \left(\tilde{n}(\lambda,T), \lambda \right) = \int_0^\infty N(r) \; Q_E \left(\tilde{n}(\lambda,T), \lambda, r \right) \; r^2 \; dr \qquad \text{2-1}$$

where

γ_E is unit volume extinction coefficient (neper m^{-1})

$N(r)$ is drop size distribution function ($cm^{-3} \; \mu m^{-1}$)

Q_E is the Mie efficiency factor for extinction

$\tilde{n}(\lambda,T)$ is the complex index of refraction (dimensionless)

λ is wavelength (cm)

r is drop radius (μm)

and T is absolute temperature ($^\circ K$)

The efficiency factor (which is a function of temperature, droplet radius, and wavelength) is obtained from the solution to the problem of diffraction of a plane monochromatic wave by a homogeneous dielectric sphere of arbitrary radius (Mie, 1908):

$$Q_E = \frac{2}{q^2} \sum_{\ell=1}^{\infty} (2\ell + 1) \ \text{Re} \left(a_\ell \ (\tilde{n}(\lambda,T),q) \ + \ b_\ell(\tilde{n}(\lambda,T),q) \right) \qquad 2\text{-}2$$

where the coefficients a_ℓ and b_ℓ in the Mie series are obtained by the boundary conditions at the surface of the sphere and at infinity, and where $q = [2\pi r/(\lambda \times 10^4)]$ is called the dimensionless drop size parameter. It is a measure of the phase shift across the droplet.

The complex index of refraction of water at centimeter wavelengths is given by the Debye Formula (1929):

$$\tilde{n}^2 = \frac{\varepsilon_o - \varepsilon_\infty}{1 + i(\lambda_0/\lambda)} + \varepsilon_\infty \ . \qquad 2\text{-}3$$

Here ε_o and ε_∞ are the static and optical dielectric constants and λ_o is the Debye relaxation wavelength. The constants are temperature dependent and their values are calculated using the values of Grant et al (1957).

Since the complex index of refraction, $\tilde{n}$, is a function of temperature and wavelength, $Q_E(\tilde{n},\lambda,r)$ must be specified for each λ and T, as well as for each r. Due to the series summation in Expression 2-2, this is not an easy matter computationally.

2.3 Rayleigh Limit - Staelin Approximation

An alternative form for the Mie extinction efficiency factor is given by a power series expansion in the dimensionless drop size parameter.

$$Q_E(\lambda,r,T) = qZ(\lambda,T) + q^3 A(\lambda,T) + q^4 B(\lambda,T) + \ldots \qquad 2\text{-}4$$

where

$$Z = 4 \ \text{Im} \ \{-K\} = 4 \ \text{Im} \left(- \frac{\tilde{n}^2 - 1}{\tilde{n}^2 + 2} \right)$$

$$A = - \frac{4}{5} \ \text{Im} \left(\frac{\tilde{n}^2 - 1}{\tilde{n}^2 + 2} \ \frac{\tilde{n}^4 + 27 \ \tilde{n}^2 + 38}{2\tilde{n}^2 + 3} \right)$$

$$B = 8/3 \ \text{Re} \left(\frac{\tilde{n}^2 - 1}{\tilde{n}^2 + 2} \right).$$

This expansion is valid for all q, but is especially useful in the limit where q << 1; i.e., when the wavelength of interest is much larger than the droplet size. At microwave wavelengths this holds true for nonprecipitating clouds.

In this limit, the Mie solution has the following asymptotic behavior:

$$q \to 0; \quad Q_E \to qZ(\lambda, T). \qquad \text{Rayleigh Limit (small droplets)}$$

For nonprecipitating clouds the average droplet radii range from 10^0 to 10^2 μm. At a wavelength of 1 cm, the q parameter is thus of the order of 10^{-3} to 10^{-2}; i.e., q << 1. This falls within the Rayleigh limit region.

Substituting into Expression 2-1,

$$\gamma_E = \int_0^\infty N(r) \, qZ(\lambda, T) \, \pi r^2 \, dr = mF(\lambda, T) \qquad 2-5$$

where

$$m = \frac{4\pi\rho}{3} \int_0^\infty N(r) \, r^3 \, dr \quad \text{is the mass density of the droplet ensemble}$$

and

$F(\lambda, T)$ is a function of wavelength and temperature only. This function has been evaluated empirically by Staelin (1966) for which the expression becomes:

$$\gamma_E = \frac{1.0016 \times 10^4 \, m \, 10^{0.0122(291-T)}}{\lambda^2} \qquad (\text{neper } m^{-1}). \qquad 2-6$$

This says that the unit volume extinction of a nonprecipitating cloud is proportional to its mass density regardless of the nature of the droplet distribution. This is not true, however, for a precipitating cloud and this approach is not applicable.

2.4 The ERT Precipitation Extinction Approximation

The approximation to be used for precipitating clouds is based on the character of the variation of $Q_E(\lambda, r, T)$ with r and the nature of the

relevant drop size distribution function $N(r)$. The upper portion of Figure 2-1 portrays the range of droplet radii for fair weather cumulus, cumulus congestus, and rain with a rainfall rate of 25.4 mm hr^{-1}. The broken line indicates the variation of Q_E (λ, r, T) with r at $\lambda = 1.0$ cm and $T = 298°K$. Note that while the size distributions of nonprecipitating clouds (Cu) are limited to the Rayleigh region, the rainfall distribution extends through the transition region to the large sphere region where the asymptotic limit of the Mie series (Expression 2-2) approaches 2:

$$q \to \infty \; ; \; Q_E \to 2. \qquad \text{Large Sphere Limit}$$

An average raindrop has a characteristic radius on the order of 10^3 μm. At a wavelength of 1 cm, the q parameter is of order 1. The Rayleigh limit is no longer valid and, furthermore, it must be recognized that the extinction factor will vary orders of magnitude within the size range of the rainfall droplets. For complete accuracy, the full Mie Theory using Eq. 2-2 should be used in this range of drop sizes. This would be feasible if all raindrops had the same radius and atmospheric temperature structure was isothermal. However, distributions of droplet radius and atmospheric vertical temperature structure make a layered computation using Eq. 2-2 computationally complex.

The approach taken here was to assume that the Mie expression (Eq. 2-4) could be approximated by a small number of terms. Also, the number of terms included was assumed to be dependent on the size range of the droplets such that the attenuation coefficient can be expressed as:

$$
\begin{aligned}
\gamma_E &= \int_0^\infty N(r) \; Q_E \; (r, \lambda, T) \; \pi r^2 \; dr \\
&\cong \int_0^{r_1} N(r) \; Q_E \; (r_1) \; \pi r^2 \; dr + \int_{r_1}^{r_2} N(r) \; Q_E \; (r_2) \; \pi r^2 \; dr \\
&+ \cdots \cdots \int_{r_n}^\infty N(r) \; Q_E \; (r_\infty) \; \pi r^2 \; dr \qquad \text{2-7}
\end{aligned}
$$

for $n + 1$ size intervals. Ideally, each of the above integrals should be expressible in closed form.

9

Based on Q_E (λ, r, T) vs. r plots such as in Figure 2-1, three representative regions were selected:

    (a) Region I   -   Rayleigh limit region $r < r_R$

    (b) Region II   -   Transition region $r_R \leq r \leq r_c$

    (c) Region III -   Large sphere region $r_c < r$

The approximations to the Mie efficiency factors in the three regions are as follows:

$$
\begin{aligned}
Q_E &= qZ & \text{for } 0 \leq r \leq r_R \\
&= qZ + Aq^3 + Bq^4 & \text{for } r_R \leq r \leq r_c \qquad\qquad 2\text{-}8 \\
&= 2 & \text{for } r \geq r_c
\end{aligned}
$$

The quantities q, Z, A, and B are as previously defined.

The limits r_c and r_R are specified in the following manner. The upper limit to the Rayleigh region is taken where the dimensionless drop size parameter reaches 0.10. This is approximately the point at which the q^3 term in Eq. 2-4 reaches 10% of the leading term in q. Thus,

$$q_R = 0.10$$

and

$$r_R = (1.59 \times 10^2)\lambda.$$

The lower limit of the large sphere region is located by specifying the position of the optical resonance region. The general criteria adopted is:

$$r_c = \frac{\lambda \times 10^4}{2|\tilde{n}|}$$

where

$$|\tilde{n}| > \pi$$

The fit of this approximation to the Mie Theory is demonstrated in Figure 2-1 and is quite reasonable.

Within the transition region bounded by (r_R, r_c), the drop size parameter takes on values in the range of $0.1 < q < 1.0$. The higher order terms Aq^3 and Bq^4, therefore, contribute significantly to the magnitude of Q_E, while higher orders in q are small corrections.

Based on this development, Expression 2-7 is truncated to a series of three integrals:

$$\gamma \simeq \int_0^{r_R} qZN(r)\ \pi r^2\ dr + \int_{r_R}^{r_c} (Aq^3 + Bq^4)\ N(r)\ \pi r^2\ dr$$

$$+ \int_{r_c}^{\infty} 2\ N(r)\ \pi r^2\ dr$$

2-9

where all the terms are as previously defined.

2.5 Drop Size Distribution Function

In order to evaluate Eq. 2-9 in closed form, the drop size distribution must be specified. The particular form of the drop size distribution $N(r)$ is empirically determined and for the purpose of our study, the most general specification for cloud droplet spectra is the Deirmendjian (1964) distribution:

$$N(r) = Ar^{C_1} \exp\{-Br^{C_2}\}$$

2-10

which characterizes the ensemble in terms of four parameters, two of which (A and B) are scale parameters, the others being shape parameters. Fair weather and stratus clouds conform nicely to this characterization. A simple form of the Deirmendjian distribution may be used to describe precipitation.

A review of the literature, especially that pertaining to radar studies of precipitation, indicated that the Marshall-Palmer (1948) model of drop size distribution for precipitation is the most appropriate for studies of satellite-measured brightness temperatures. The virtues of this model are that: (1) an empirical expression exists which relates the drop size

11

distribution (useful in computations of radiative interaction) to the instantaneous rainfall rate (useful in synoptic studies), and (2) the form of the expression is essentially that of the Deirmendjian expression used in modeling cloud droplet distributions. The Marshall-Palmer model is expressed as:

$$N(r,R) = k_1 \exp - \{k_2 \, rR^{-k_3}\} \qquad \qquad 2\text{-}11$$

where

$$k_1 = 8.0 \times 10^{-6}$$
$$k_2 = 8.156 \times 10^{-3}$$
$$k_3 = 0.21$$

and

$N(r,R)$ is the number density of particles per unit size range $(cm^{-3} \mu m^1)$

r   is the droplet radius (µm) for a given rain rate.

R   is the rainfall rate (mm/hr).

This is essentially the Deirmendjian distribution with parameters:

$$A = k_1$$

$$B = k_2 R^{-k_3}$$
$$C_1 = 0$$
$$C_2 = 1$$

Substituting Eq. 2-11 into Eq. 2-9 and evaluating, the extinction coefficient becomes a function of wavelength, temperature, and rainfall rate:

$$\gamma(\lambda,T,R) = \sum_{n=1}^{7} C_n \, F_n(\lambda) \, G_n(\lambda,T) \, H_n(\lambda,R) \, R^{0.21n} \qquad \qquad 2\text{-}12$$

where

C_N are constants

and

F_N, G_N, H_N are functions of the indicated variables.

2.6 Discussion of the Approximation

The derived expression for the extinction coefficient $\gamma(\lambda,T,R)$ is essentially a power series in the rainfall rate, R, with lowest term going as $R^{0.21}$ and highest term going as $R^{1.47}$. Temperature and wavelength dependence are given by the coefficients in this finite series. It can be shown that this solution reduces to the Staelin approximation in the limit as the rainfall rate approaches zero. This limit is demonstrated in Figure 2-2 giving the dependence of extinction coefficient on temperature at low rainfall rates (R = 0 and 1 mm hr^{-1}) and at an intermediate rainfall rate (R = 39.5 mm hr^{-1}). Note that although the intermediate rates are essentially temperature independent, there is a marked variation (by a factor of 4 to 5) at lower rainfall rates. Additionally, the extinction due to the cloud alone (R = 0) is typically an order of magnitude less than that due to medium precipitation (R = 39.5 mm hr^{-1}). The importance of the cloud contribution decreases with increasing temperature. Comparisons between the approximation and both Mie Theory and the Staelin Formula (Rayleigh scattering) can be made. Various authors have made full Mie computations at radar wavelengths based on convolution with the Marshall-Palmer distribution. Wexler and Atlas (1963) and Shifrin and Chernyak (1968) have demonstrated that the volume extinction coefficient is a near-linear function of rainfall rate. This behavior is reproduced by the approximation. Figure 2-3 demonstrates the extinction vs. rainfall rate relationship at $\lambda = 1.35$ cm, T = 283°K for full Mie Theory, the precipitation approximation, and the Staelin Formula. The extreme underestimation of the extinction by the Staelin approximation is due to the total neglect of scattering and higher order absorption by the Rayleigh approximation. The precipitation approximation includes these effects to first order and improves to within 85% of the full Mie series solution for the worse case at 60 mm/hr. Figure 2-4 compares three radar extinction vs. rainfall rate results with the approximation. On the basis of these calculations it is concluded that the approximation significantly improves the rainfall rate dependence of the extinction coefficient predicted by the Staelin Formula, approaching the behavior of the full Mie series solution.

The frequency dependence of the extinction coefficient is significant in determining information retrievable from multispectral analysis. Figure

13

2-5 demonstrates the frequency dependence of the ERT approximation as compared to the Staelin Formula (Rayleigh Scattering-only curve) and two full Mie Theory calculations: (1) a Deirmendjian distribution (parameters $C_1 = 5.0$, $C_2 = 0.6$) with a mode radius of 400 μm and a mass density of 1.0 g m^{-3}; and (2) a Marshall-Palmer distribution with a mass density of 1 g m^{-3}. Figure 2-5 demonstrates that the approximation models the frequency dependence of full Mie Theory calculations quite well.

Figure 2-2 Reduction of the ERT Approximation to the Staelin Formula as the Rainfall Rate Approaches Zero

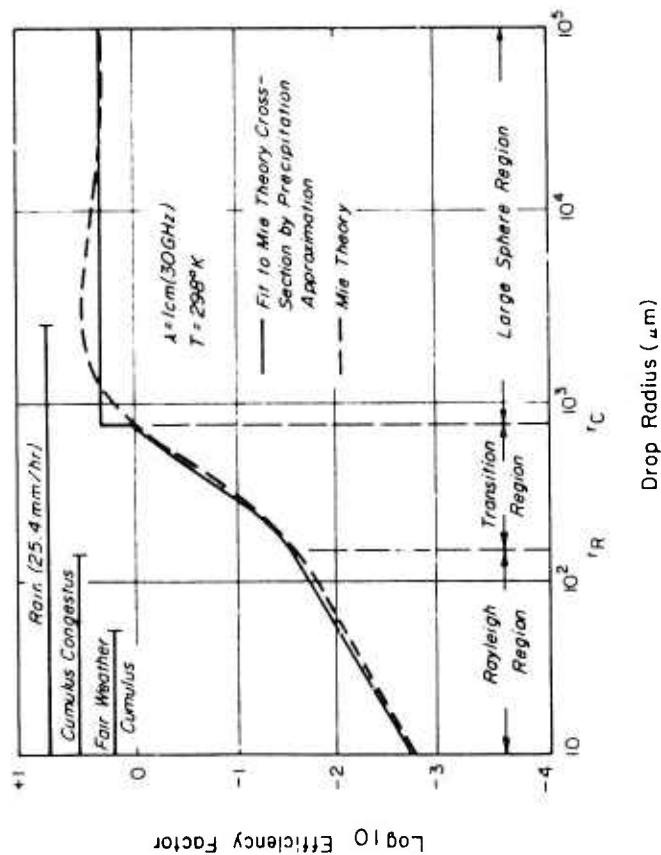Figure 2-1 Range of Drop Sizes and Mie Efficiency Factors for Full Mie Theory and Linear Segment Approximation

15

Figure 2-4 Comparison Between Full Mie Theory and the ERT Approximation
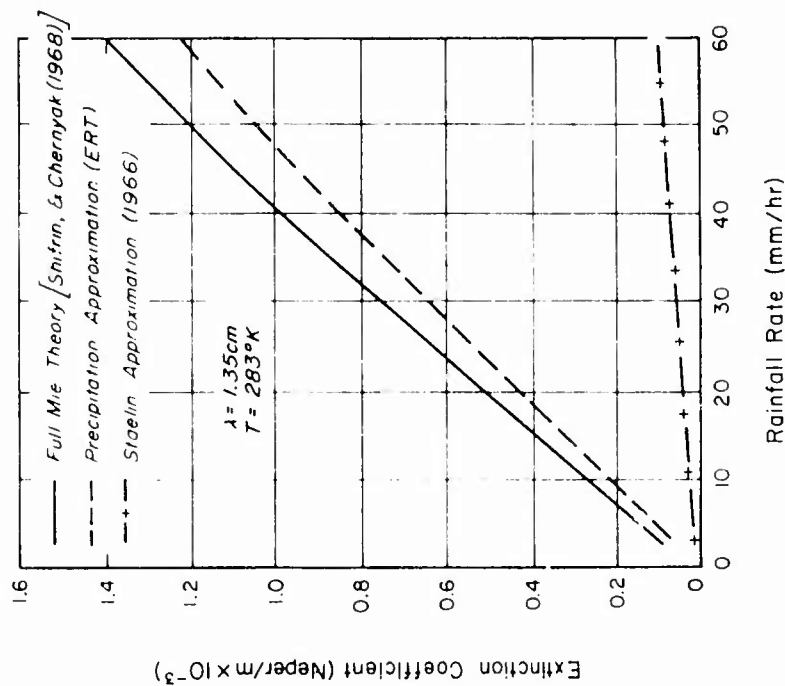

Figure 2-3 Comparison of the Extinction Coefficient Using the Staelin Formula, the ERT Approximation, and Full Mie Theory
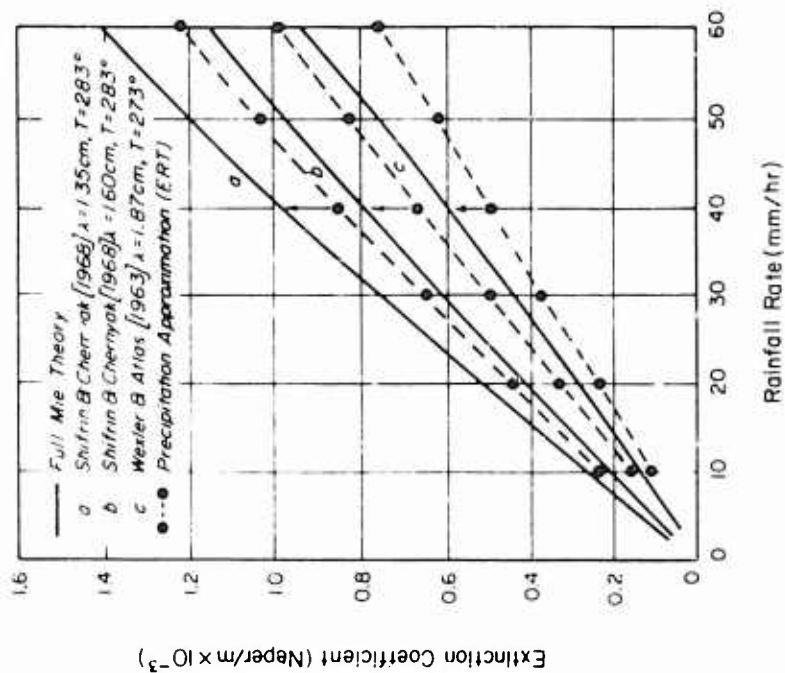
16
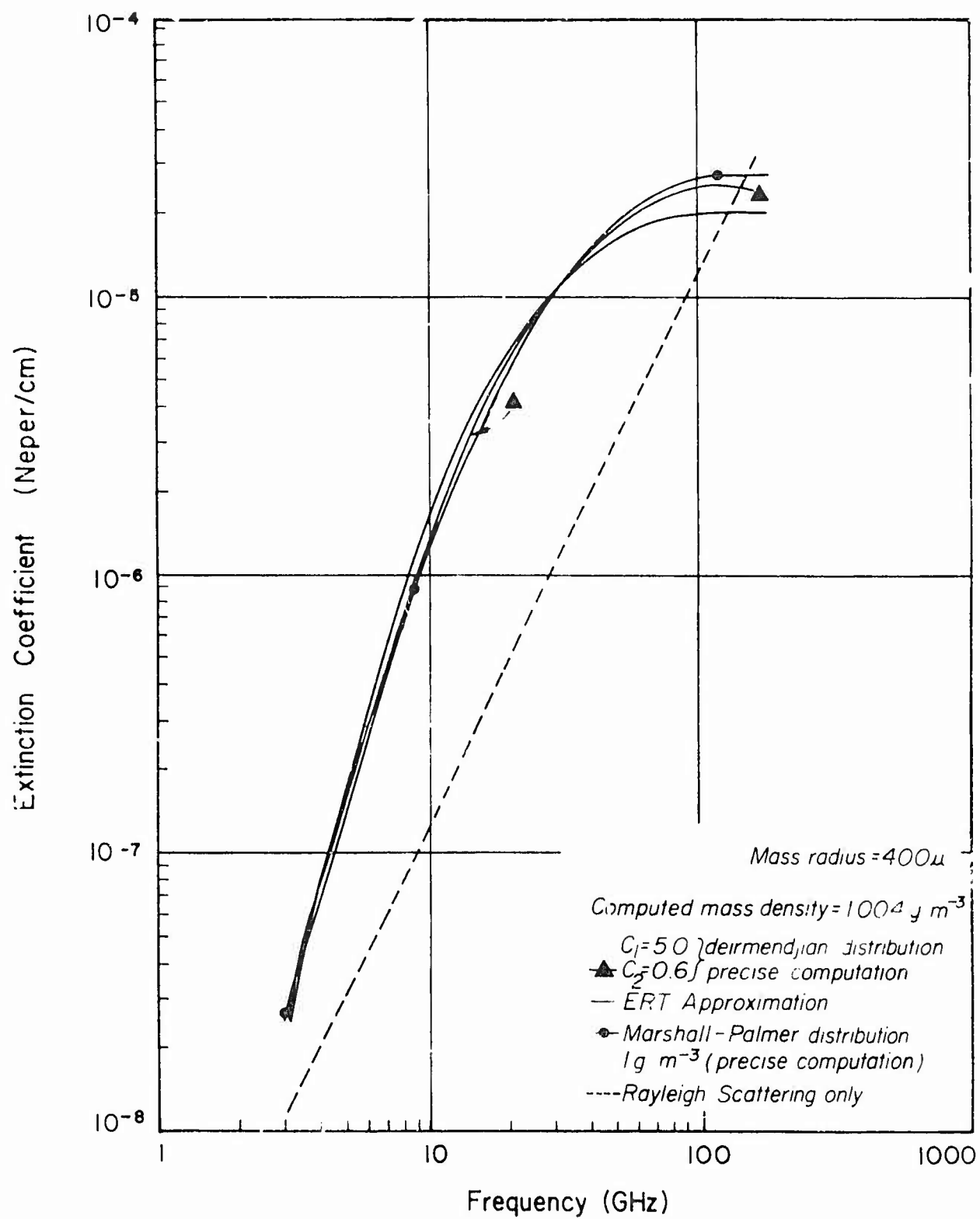
Figure 2-5   Frequency Dependence of the Extinction Coefficient for
Various Models

17

3. TEMPERATURE PROFILING ANALYSIS

3.1 Scope

Aspects of atmospheric temperature profiling by passive microwave techniques were systematically analyzed. These included the following:

- Effects of line shape model on the computation of weighting functions and, therefore, simulated brightness temperatures.

- Comparison of the use of the 118 GHz O_2 complex in temperature profile with that of the 60 GHz O_2 complex.

- Evaluation of the effects of clouds and precipitation on temperature profiling in the two spectral regions.

The results of these analyses are presented in this section.

3.2 Approach

3.2.1 Line Shape Analysis

Previously, the ERT simulation programs made use of the Van Vleck-Weisskopf line shape model. For this study, the Gross-Reber model was adopted. Evaluations of this change on temperature profiling simulation results were performed by comparing the differences in absorption computed using the two models. Computations were made at a number of frequencies and at a number of pressures and concentrations. In addition, typical weighting functions were computed using the models and compared.

3.2.2 Temperature Profiling Analysis

The remaining two tasks identified previously were accomplished by simulation inversion analysis using ERT programs. The inversion procedure, the statistical method for estimation of parameters, has been well documented in previous reports such as Gaut, Reifenstein and Chang (1972). This procedure is shown schematically in Figure 3-1. Briefly, the approach uses physical and interaction models operating on an ensemble of atmospheric data (including clouds and precipitation) to create a correlation matrix

Preceding page blank

19

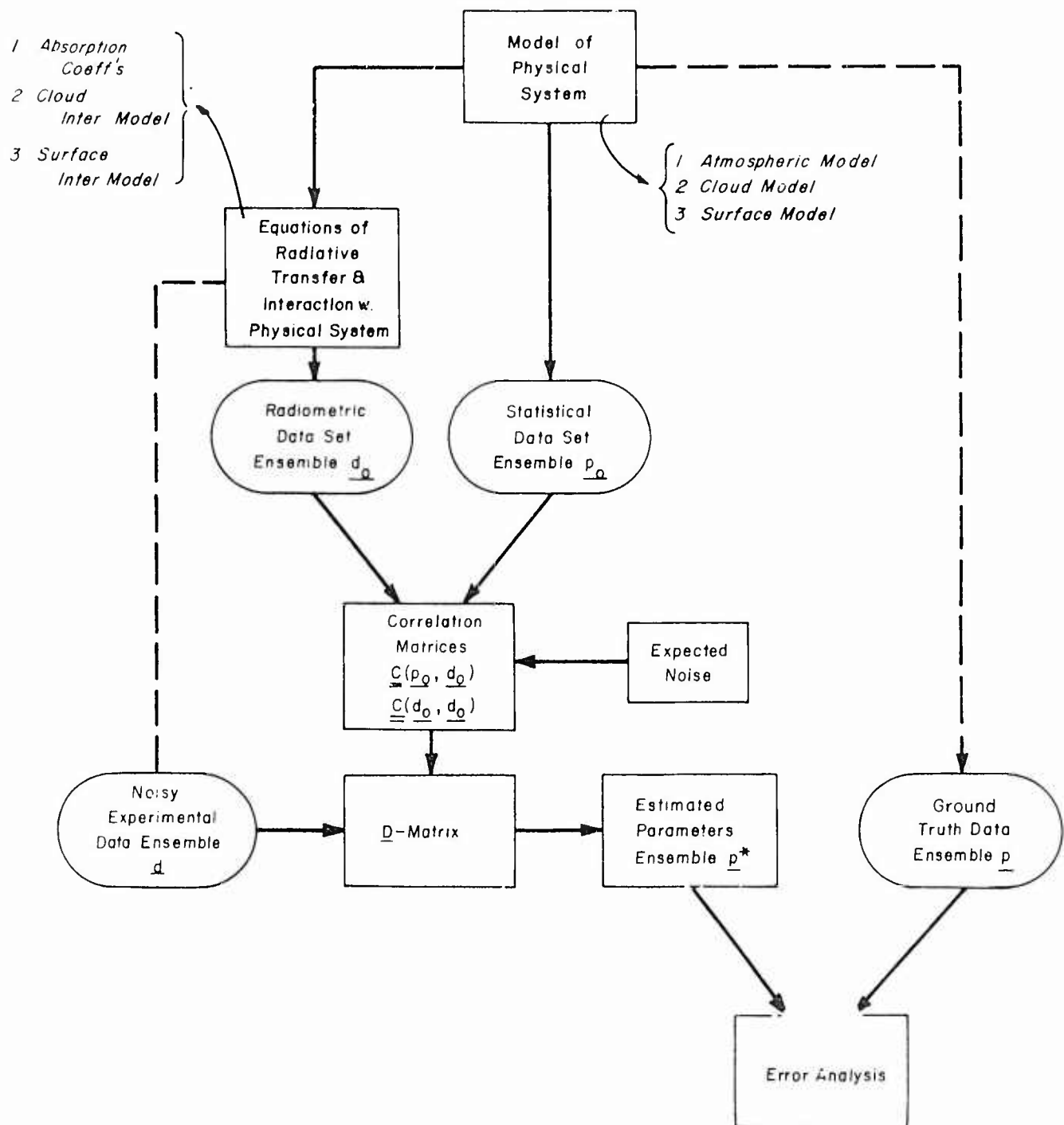Figure 3-1 Flow Diagram for Application of the Data Inversion Methodology to Parameter Estimation for a Radiometric Experiment. (The p and d data sets may be simulated for study purposes, as shown by dashed lines.)

20

or "D-Matrix" between brightness temperatures at selected frequencies and geophysical parameters of interest. This so-called D-Matrix is then used to "infer" from actual radiometric measurements the values of the corresponding geophysical parameters. In the analysis and evaluation made where real radiometric measurements are not available, a simulation procedure is used to generate a set of "experimental data." The simulation procedure used is identical to that used to generate the data for the D-Matrix. However, a separate and different ensemble of atmospheric and surface data is used for this evaluation data set.

For the purposes of this study actual historic radiosonde data were used to describe the vertically correlated temperature structure of the atmosphere. Similarly, radiosonde data were used to specify the vertical distribution of atmospheric water vapor. Since radiosonde data do not contain basic information on the presence and types of clouds, these have to be inserted according to some realistic procedure. Statistics of the probability of occurrence for each of six major cloud categories (including clear-sky conditions) corresponding to the season and locations of the radiosonde data were used, together with a random number generator, to insert the proper distribution of clouds into the ensemble of radiosonde data. Each of the major cloud types has a physical description in terms of its vertical extent, drop size distribution and liquid water content. These parameters are, in fact, the ones which get inserted into the radiosonde profiles to create the ensemble of atmospheric data.

In some of the analyses performed for this study, a different approach was adopted in creating ensembles of atmospheric data for evaluation. In order to clearly identify the effects of clouds and precipitation on inversion results, different ensembles of atmospheric data were created, using the same set of temperature profiles, to represent conditions with:

- Clear sky
- A cloud with fixed thickness and liquid water content
- Precipitation with fixed liquid water content

Each of these ensembles were "inverted" using the same D-Matrix that was created using cloud and precipitation conditions representative of the season and station location. By comparing the inversion results either in

terms of the ensemble statistical rms errors or in terms of individual profile accuracies, the effects of clouds and rain (and, therefore, drop size) can be isolated.

3.3 The Attenuation Due to Oxygen

The attenuation of microwave radiation near frequencies of 60 GHz and 118 GHz is due primarily to the resonance of oxygen molecules. These resonances, caused by magnetic dipole rotational transitions, occur at several frequencies within the 50 to 60 GHz range and at 118.7505 GHz. Each resonance line has a line width related to the radiation transition lifetime which is broadened by molecular collisions in a manner which is pressure and temperature dependent. As a result, the individual lines between 50 and 60 GHz are clearly defined at very low pressures, but combine to form a continuous absorption region at pressures of one atmosphere.

To compute the microwave absorption coefficient due to oxygen, it is necessary to sum the absorption caused by each rotational state found in appreciable populations at atmospheric temperatures. This requires knowledge of the line shapes and line width parameters, information which is currently provided from theory but must be empirically supported. Previous studies at ERT have followed the approach presented by Meeks and Lilley (1963) using their line-width expression with the line-shape factor defined by Van Vleck and Weisskopf (1945) to determine the contribution of each resonance line to the absorption coefficient. However, recent research (e.g., Reber, 1972), has indicated that the form factor developed by Gross (1955) agrees more accurately with measurements of microwave attenuation. The Gross line shape was thus adopted for this study and comparisons were made between the attenuation predicted by the Van Vleck-Weisskopf expression and by the Gross form factor.

3.3.1 The Oxygen Line Shapes

The theory behind collision broadening of spectral lines was first developed by Lorentz (1909) for resonant phenomena at optical wavelengths and by Debye (1929) for nonresonant phenomena. Van Vleck and Weisskopf (1945) analyzed and reformulated their theories to derive a general formula for the absorption coefficient based upon an assumption of strong molecular

22

collisions. As a result of their research, the following line-shape expression was derived:

$$F(\nu, \nu_n) = \frac{\Delta\nu}{(\nu_n - \nu)^2 + \Delta\nu^2} + \frac{\Delta\nu}{(\nu_n + \nu)^2 + \Delta\nu^2} \qquad 3\text{-}1$$

where

ν = observation frequency (GHz)

ν_n = resonant frequency of the nth rotational transition (GHz)

$\Delta\nu$ = line width

Gross (1955) reexamined all of the above theories and the assumptions upon which they were based. In the Van Vleck-Weisskopf approach, molecular collisions were assumed to leave the oscillator positions and velocities distributed according to the Boltzmann distribution appropriate to the applied field at the time of collision. Gross showed that this required unrealistically large oscillator velocities and that the theory failed at zero and infinite frequencies. He thus modified the theory by assuming that the oscillator positions are unchanged as a result of collision, but that the velocities are altered to the Boltzmann distribution corresponding to the time of impact. This led to a reformulation of the form factor:

$$F(\nu, \nu_n) = \frac{4\nu_n^2 \, \Delta\nu}{(\nu_n^2 - \nu^2)^2 + 4\nu^2 \Delta\nu^2} \qquad 3\text{-}2$$

where the variables are defined above.

Reber (1972) made an extensive series of measurements of zenith atmospheric attenuation in the 50 to 70 GHz range and compared his results with those predicted by the Lorentz, Van Vleck-Weisskopf and Gross form factors. Fitting the theoretical values to his data, he found that the Gross and Lorentz line shape resulted in an rms error of 8.24% and 8.25%, respectively. The Van Vleck-Weisskopf line shape, on the other hand, showed an rms error of 13.70%. He also showed that the Van Vleck-Weisskopf form factor, while generally agreeing with the others between 50 and 60 GHz, skews the total attenuation curve, especially above 60 GHz, and that at 70.26 GHz, it predicts 30 to 40% more zenith attenuation than his measured values showed.

23

3.3.2 A Comparison Between the Van Vleck-Weisskopf and the Gross Line Shapes

To determine the effect of the differences between the Van Vleck-Weisskopf and Gross line shapes on the simulation of atmospheric attenuation, computations of the oxygen absorption coefficient, γ, were made at 1 GHz intervals from 30 to 130 GHz for pressures representative of the atmosphere. These are shown in Figure 3-2 for the Van Vleck-Weisskopf line shape and in Figure 3-3 for the Gross line shape. Excellent agreement is seen near 60 GHz and 119 GHz where the resonant frequencies occur, since the two formulations agree in value on the oxygen lines. It thus appears that for near-resonance microwave channels, either line shape provides a good absorption prediction.

Away from the oxygen lines, significant differences are found between the two expressions. Below 35 GHz the Van Vleck-Weisskopf expression estimates attenuation above that predicted by the Gross expression, while between 35 GHz and 50 GHz it predicts coefficients lower than those predicted by Gross, although remaining within 10% of the value. More pronounced differences are found between 65 GHz and 110 GHz, since in this frequency range the Van Vleck-Weisskopf absorption coefficient far exceeds the Gross one. This is especially true above 85 GHz where the coefficients disagree by a factor of 2. These results are in line with the findings of Reber (1972) discussed above and indicate that the use of the Gross line shape for non-resonant frequencies is of great importance to an accurate simulation of atmospheric attenuation.

Figures 3-4 and 3-5 show the weighting functions computed from the two expressions for frequencies of 53.29 GHz and 54.3 GHz, respectively. These were generated by the simulation program for a tropical atmosphere over a calm ocean. Both of these frequencies are near line centers and, as would be expected from the analysis given above, show no significant differences. Similar agreement was found for other channels in the 50 to 60 GHz range and near 118 GHz, indicating that the inversion for atmospheric temperature should provide the same results using either the Van Vleck-Weisskopf or the Gross line shape. However, temperature inversions are often performed simultaneously with inversions for water vapor or liquid water using channels away from the oxygen lines. Thus, the Gross line shape was incorporated into the INVERT programs to provide the maximum accuracy in the simulation of radiative transfer.
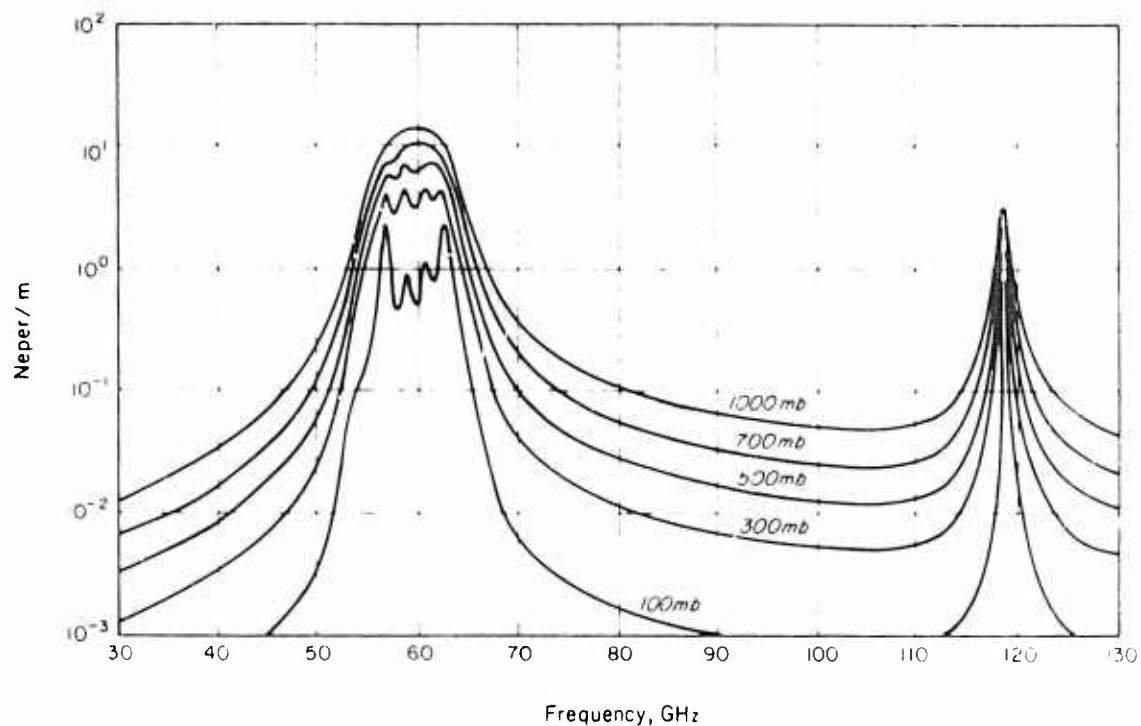
Figure 3-2   Atmospheric Oxygen Attenuation, Van Vleck-Weisskopf Line Shape
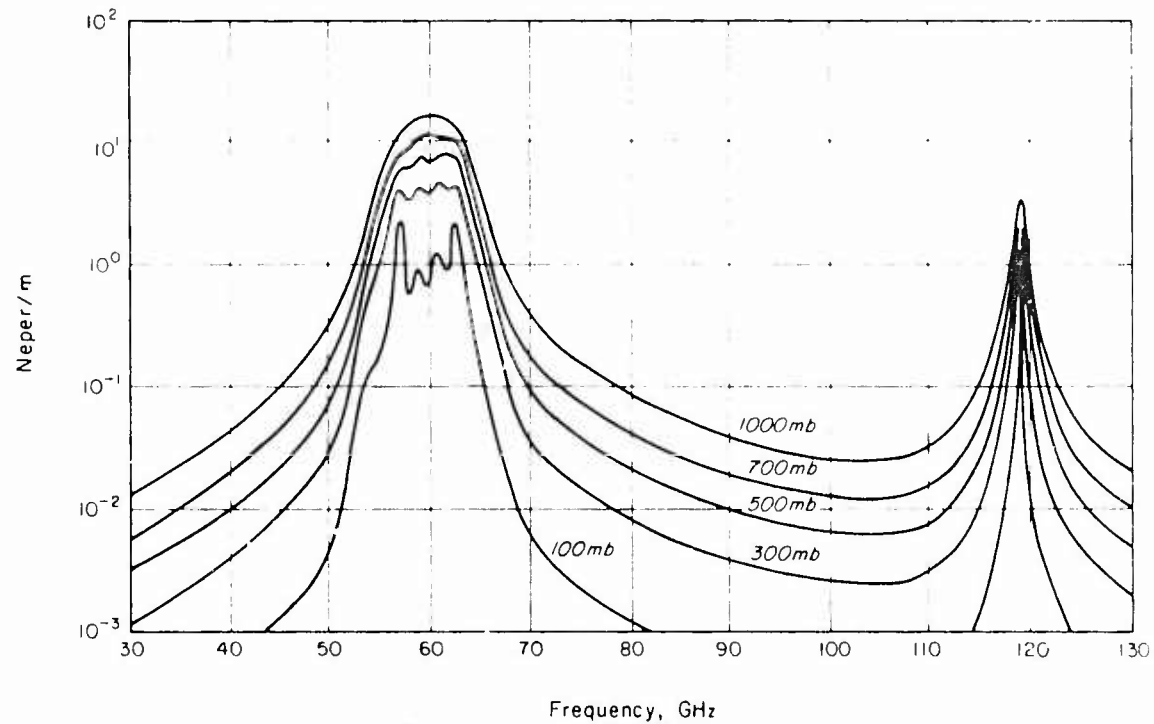

Figure 3-3   Atmospheric Oxygen Attenuation, Gross Line Shape
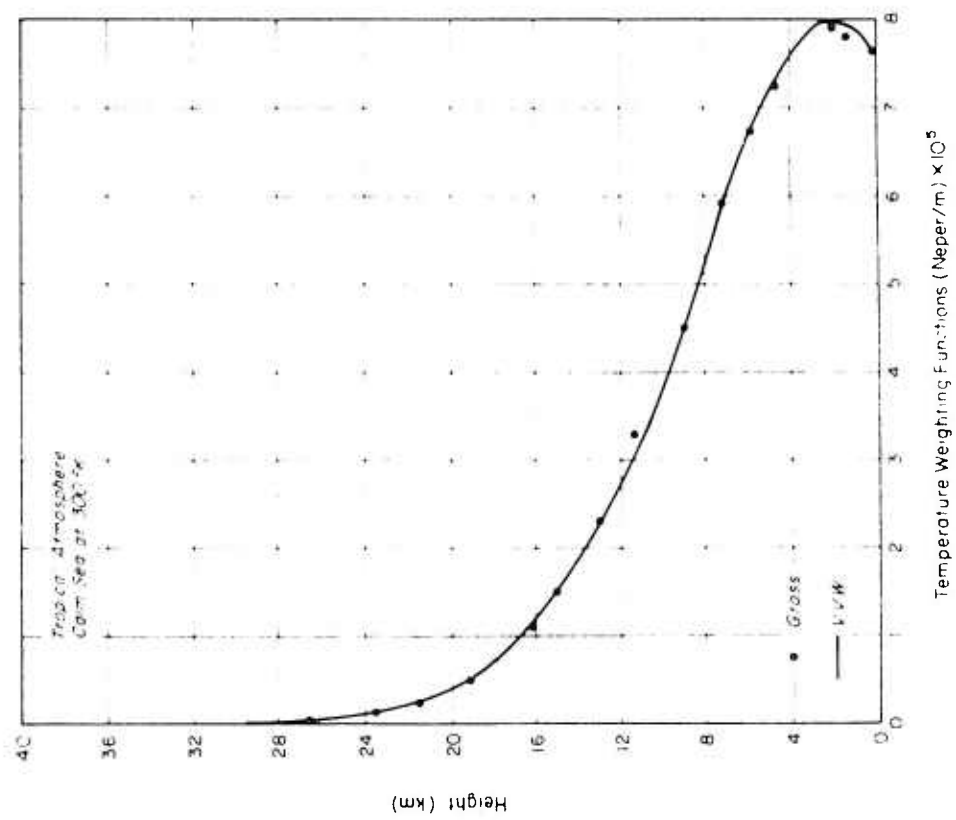
25

Figure 3-5 Comparison of the Van Vleck-Weisskopf and Gross Temperature Weighting Functions for the 54.30 GHz Channel
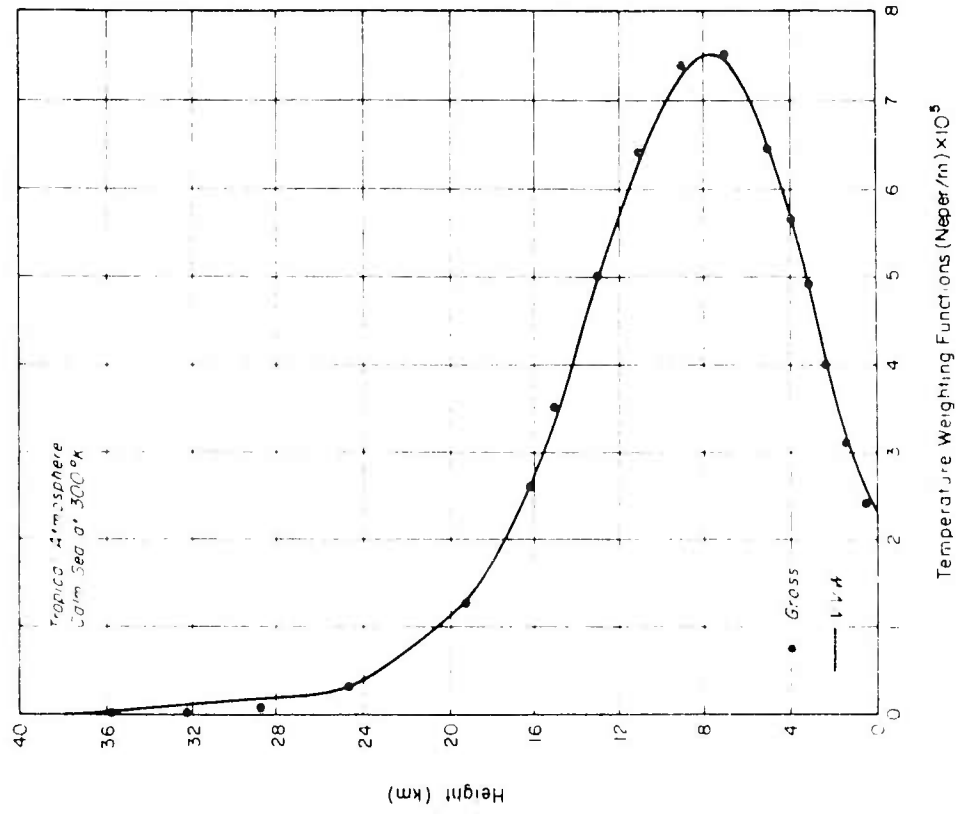

Figure 3-4 Comparison of the Van Vleck-Weisskopf and Gross Temperature Weighting Functions for the 53.29 GHz Channel

26

3.4   Inversion Analysis Results

3.4.1   Selection of Spectral Channels

The starting point of the analysis was the set of five channels in the
60 GHz complex previously selected by ERT as appropriate for temperature
profiling in the troposphere and lower stratosphere. These channels are
shown in Figure 3-6 in terms of their weighting function computed for mid-
latitude (Figure 3-6a) and for tropical (Figure 3-6b) clear-sky conditions
with an ocean background. The peaks of the weighting functions are located
at approximately 2, 7, 13, 17 and 23 km and do not appear to differ signifi-
cantly between the tropical and midlatitude conditions. The shape of the
weighting function for the 58.80 GHz channel with peak value at 17 km appears
compressed with a higher maximum in the tropical case due to the effect of
the tropical tropopause which is located at approximately this altitude.

Comparable channels were sought in the wing of the 118 GHz line, where
difficulty was encountered in defining a channel with a peak value corre-
sponding to that of the 53.29 GHz line; i.e., with peak at about 2 km. The
selected set of frequencies and their corresponding weighting functions is
graphically illustrated in Figure 3-7, with the midlatitude ocean case shown
in Figure 3-7a and the tropical ocean case in Figure 3-7b. Compared to the
corresponding weighting functions for the 60 GHz channels, it is clear that
with the exception of the 117.76 GHz channel, the match between the two sets
of weighting functions is quite good. Further analysis of the 117.76 GHz
channel suggests that the difficulty in defining a channel with peak at
low altitudes is due to the strong effects of water vapor attenuation con-
tributed by the 183 GHz water vapor line. Figure 3-8 shows the weighting
functions for the same set of frequencies, but computed for a dry atmo-
sphere; i.e., with integrated water vapor of 0 g cm^2. Under this condition,
the 117.76 GHz channel peaks at approximately 2 km and the change in the
118 GHz channel is also significant. Changes in the weighting functions
for the other channels are less apparent due to the fact that the water
vapor in the atmosphere occurs mainly at levels below 5 km.
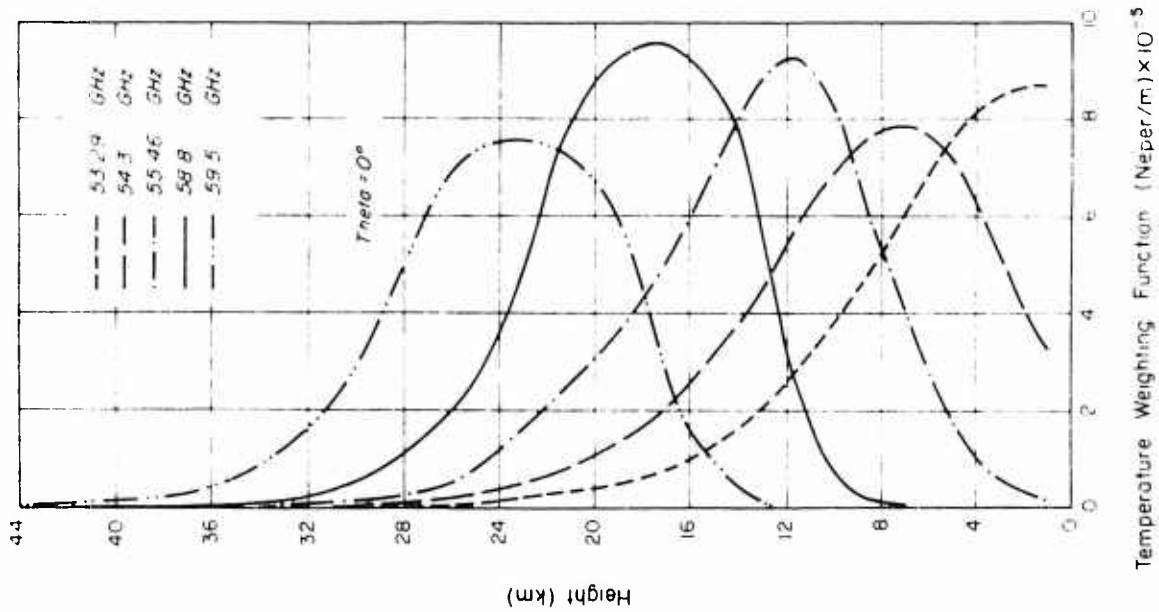
Temperature Weighting Function (Neper/m) ×10⁻⁵
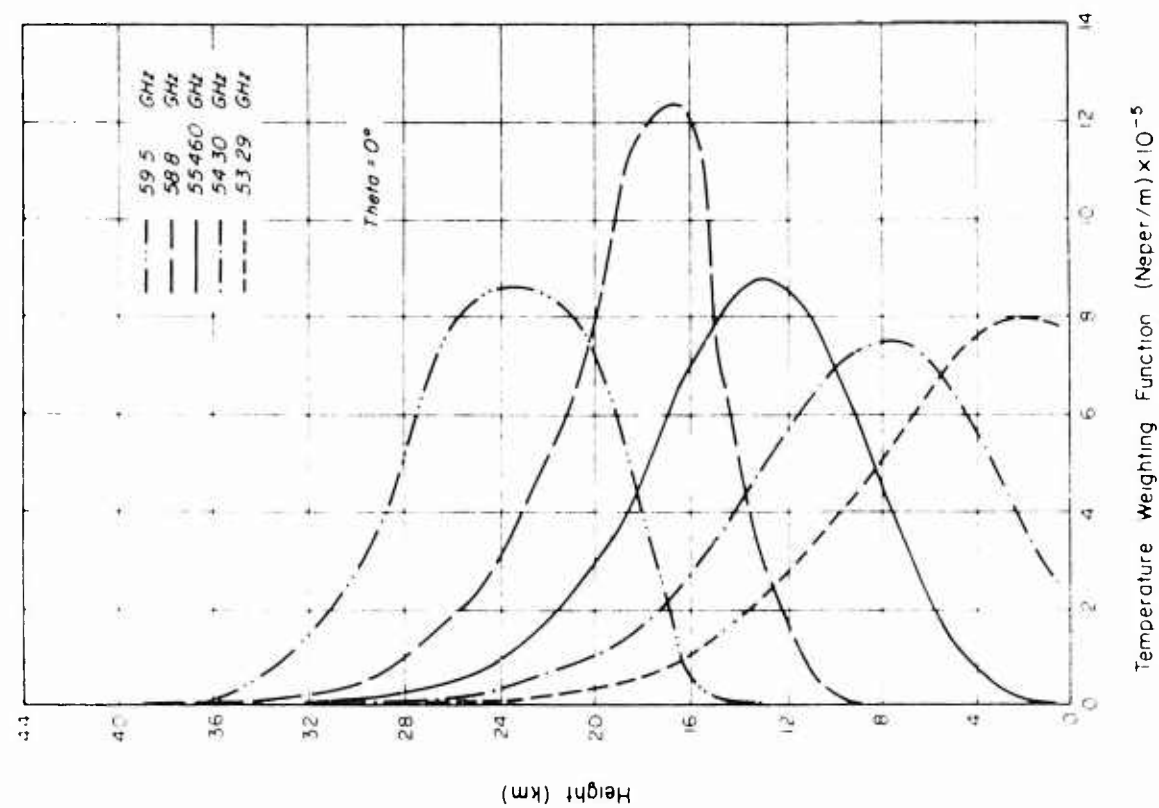
b) Tropical Atmospheric Conditions with Integrated Water Vapor of 4 g cm⁻²

Height (km)

Temperature Weighting Function (Neper/m) ×10⁻⁵

a) Midlatitude Conditions with Integrated Water Vapor of 1.6 g cm⁻²

Height (km)

Figure 3-6. Temperature Weighting Functions for Channels in the 60 GHz Complex

Temperature Weighting Function (Neper/m) × 10^-5

b) Tropical Conditions with Integrated Water Vapor of 4 g cm^-2

Figure 3-7 Temperature Weighting Functions for Channels near the 118 GHz line

Temperature Weighting Function (Neper/m) × 10^-5

a) Midlatitude Conditions with Integrated Water Vapor of 1.6 g cm^-2

29
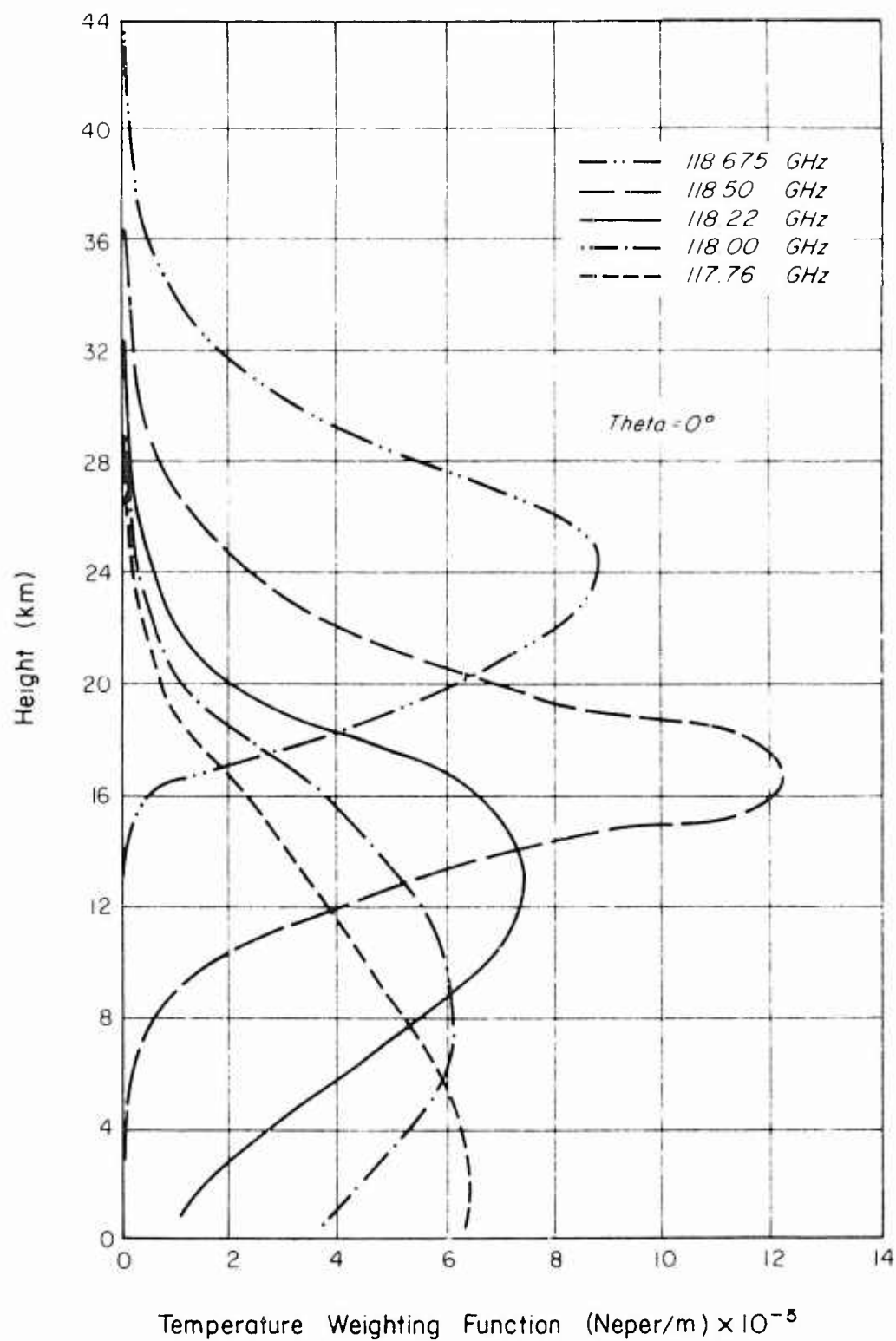
Figure 3-8 Temperature Weighting Functions for the 118 GHz Channels Computed for a Dry Tropical Atmosphere

Legend:
- — ·· — 118 675 GHz
- — — 118 50 GHz
- —— 118 22 GHz
- — · — 118 00 GHz
- — — 117.76 GHz

Theta = 0°

Height (km)

Temperature Weighting Function (Neper/m) × 10^{-5}

3.4.2 Temperature Inversion Results: The General Case

A set of general inversion analyses was performed using the 60 GHz and the 118 GHz channels separately, with cloud statistics appropriate to the selected regions and seasons. Also included in these analyses were channels selected to probe for water vapor and cloud liquid water. Table 3-1 summarizes the two sets of frequencies used. In all of the downlooking cases, the channels were nadir viewing. In the uplooking cases, the instruments sensed directly at zenith.

TABLE 3-1

FREQUENCIES SELECTED FOR ANALYSIS OF THE GENERAL CASE

Purpose	$\nu < 60$ (GHz)	$\nu > 117$ (GHz)
Temperature Profiling	53.29	117.76
	54.30	118.00
	55.46	118.22
	58.80	118.5
	59.50	118.675
Water Vapor and Liquid Water	18.0	18.0
	21.0	21.0
	22.235	22.235
	31.6	31.6

Inversion analysis was performed for two climatic conditions: midlatitude spring and tropical summer. Spring in the midlatitudes is a season of rapid and frequent changes in air masses, and thus in atmospheric temperature and moisture structures. Data from this climatic regime is thus representative of a high degree of atmospheric variability. Climatic conditions in the tropics, on the other hand, are quite stable and the natural variability in both temperature and moisture is quite small.

The inversion results for the downward-looking cases are shown in Figures 3-9 to 3-12, expressed as rms errors. The midlatitude analysis

31

was performed using a D-Matrix generated from 84 atmospheric profiles and evaluated against 36 simulated measurement sets. The tropical analysis used a D-Matrix generated from 76 atmospheric profiles and evaluated against 36 simulated measurements sets. In each case, the data plotted represent the rms difference for the 36 evaluation samples between the inversion results and the input profile values. Also shown are the expected a priori variability of each of the parameters at each level in the atmosphere. These a priori values, computed from the data used to create the D-Matrices, can be interpreted as the rms error which would result if the profiles were simply "guessed at" based on climatology alone. The differences between the a priori variability and the inversion rms error is a measure of the improvement of the results inferred from radiometric measurements over those estimated from climatological data.

In examining the figures, the differences in the variability between the tropical and midlatitude spring atmospheres are clearly reflected in the a priori statistics. In the tropospheric levels the rms variability of temperature for the midlatitude case is approximately 7°K, while for the same altitude region, the rms variability of the tropical atmosphere is only of the order of 1°K. A similar difference exists for the moisture profiles, especially at the lower levels. Because of this difference in a priori variability, it can be expected that remote sensing data are more useful in the midlatitude zones. The results of the error analysis shown in these figures, in fact, demonstrate this phenomenon. For the midlatitude situation, either of the channel combinations reduces the rms error in estimating temperature profiles by some 5°K to 6°K over climatology in the tropospheric layer above 2 km, while the differences between the inversion rms error and a priori statistics for the tropical temperature case is only near 1°K.

In comparing the midlatitude results obtained using the higher frequency oxygen channels with those using the 60 GHz channels, it is evident that at levels below 6 km the higher frequency channels are not as effective in measuring temperature. This difference is probably a direct result of the fact that the weighting functions for the set of channels in the 118 GHz line were shown to be sensitive to atmospheric water vapor.
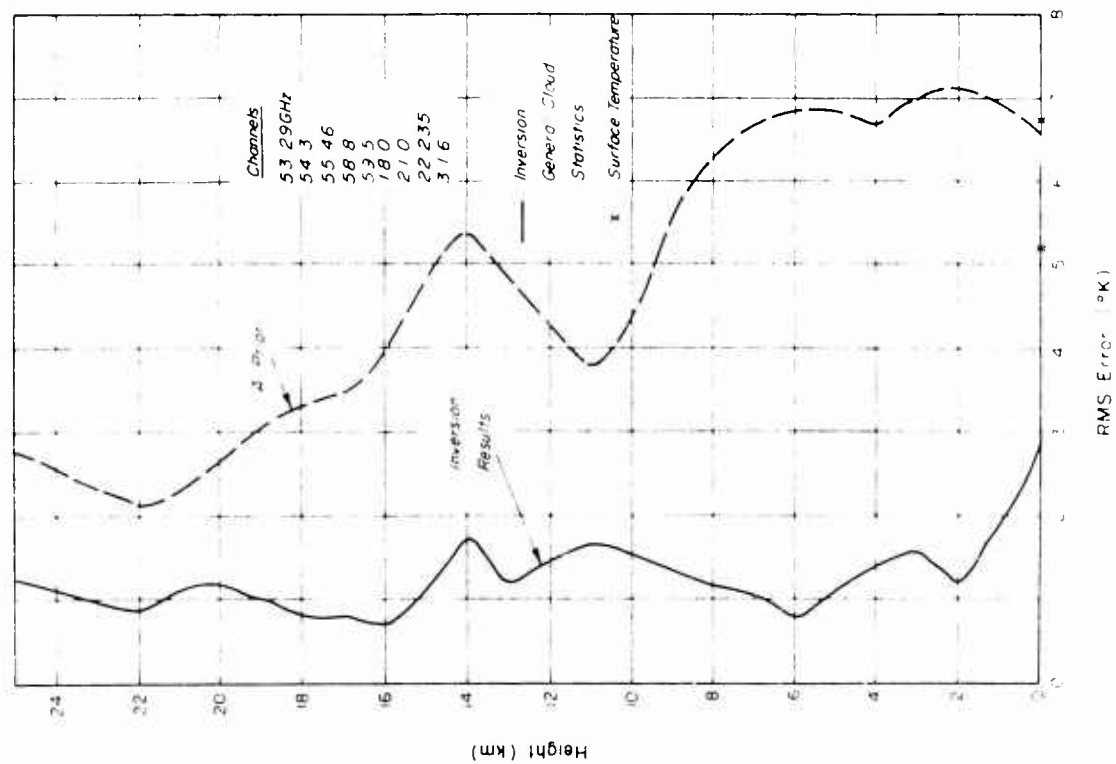
b) Liquid Water Content and Water Vapor $(g\ cm^{-2})$
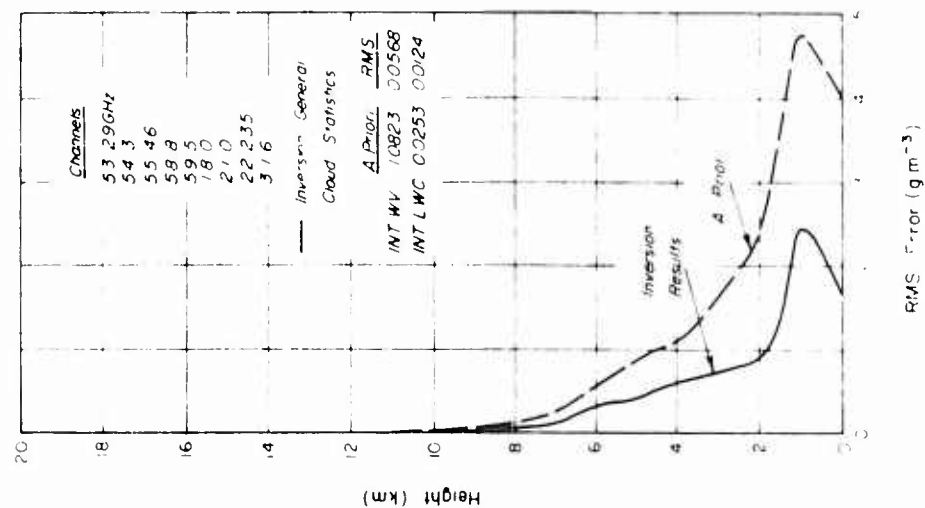
a) Temperature Inversion Results

Figure 3-9 Inversion Results for the Midlatitude Case with General Cloud Statistics Using Channels in the 60 GHz Complex

RMS Error (g m⁻³)

Inversion Results	A Priori	RMS
INT WV	10823	00598
INT LWC	00253	00:28

Channels

117 76GHz
118 0
118 22
118 5
118 675
118 0
21 0
22 235
3 / 6

A Priori

Inversion
Results

Height (km)
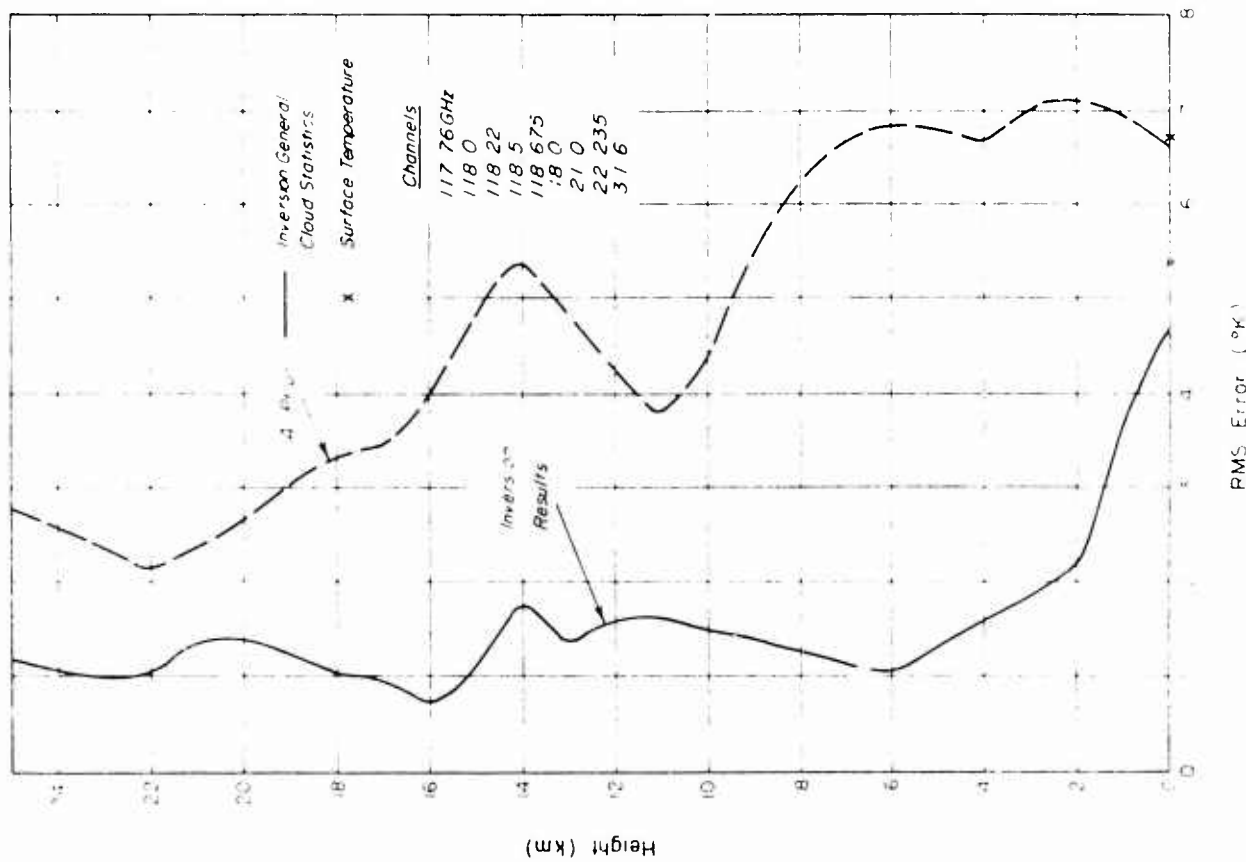
b) Water Vapor Density Inversion Results,
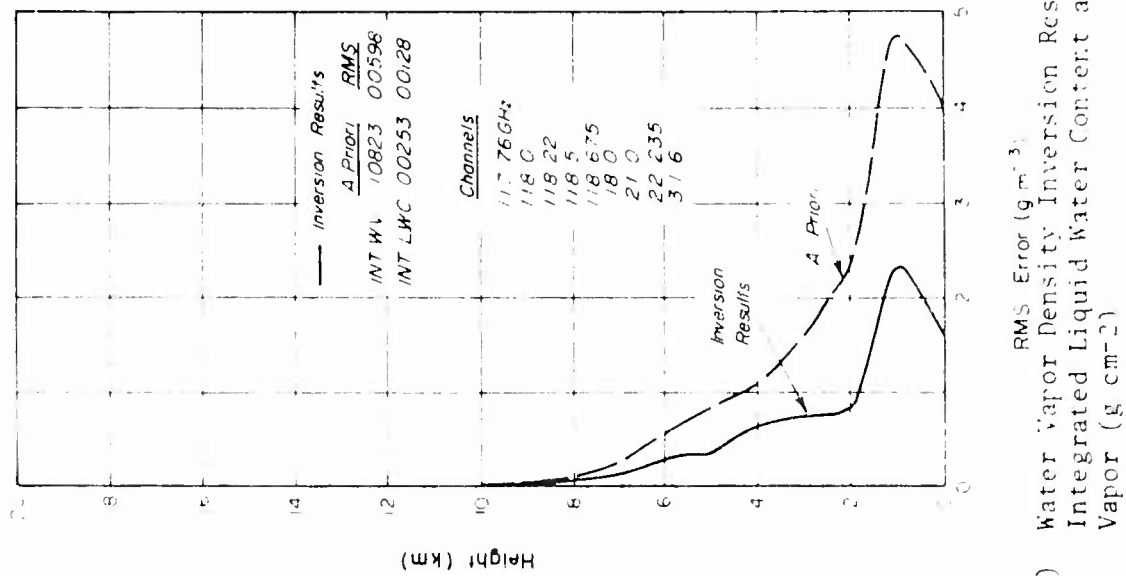Integrated Liquid Water Content and Water
Vapor (g cm⁻²)

Figure 5-10 Inversion Results for the Midlatitude Case with General Cloud Statistics Using Channels near
the 118 GHz Line

Inversion General
Cloud Statistics

Surface Temperature

×

Channels

117 76GHz
118 0
118 22
118 5
118 675
;18 0
21 0
22 235
3 / 6

A Priori

Inversion
Results

RMS Error (°K)

Height (km)

a) Temperature Inversion Results

Figure 3-11 Inversion Results for the Tropical Case with General Cloud Statistics Using Channels in the 60 GHz Complex

a) Temperature Inversion Results

b) Water Vapor Density Inversion Results, and Integrated Liquid Water Content and Water Vapor $(g \ cm^{-2})$

b) Water Vapor Density Inversion Results, and Integrated Liquid Water Content and Water Vapor (g cm⁻²)

a) Temperature Inversion Results

Figure 3-12 Inversion Results for the Tropical Case with General Cloud Statistics Using Channels near the 118 GHz Line

36

Above 6 km, where water vapor exists at highly reduced concentration, no substantial difference between the two sets of channels is evident.

Inversion error analysis was also performed for the upward-looking case using the same sets of channels. Computations were made only for the midlatitude spring climatic condition. The results are shown in Figure 3-13 and Figure 3-14. Since these channels were not in any sense optimized for the upward-looking situations, it is surprising to note the relatively good performance of the 60 GHz channels in the lower and midtroposphere with inversion rms errors in temperature of < 1.5°K up to 6 km. The relatively poorer performance of the 118 GHz channels in tropospheric temperature probing is, again, evident in the upward-looking case.

3.4.3 Effects of Clouds and Rain on Temperature Profiling

The results discussed in Section 3.4.2 are based on a D-Matrix with atmospheric profiles which include clouds where the frequency of occurrence corresponds to the climatological conditions appropriate to the location and season. Similarly, the evaluation data sets of 36 profiles also contained cases with various cloud types. However, the evaluation sample was too small to permit a systematic evaluation of the effects of clouds on inversion result accuracies, so new data sets were created with clouds and precipitation of known properties systematically inserted into the temperature profiles. This made it possible to isolate the effects of cloud thickness, cloud liquid water content, and cloud height on temperature inversion accuracies.

As a preliminary to the actual inversion analysis, computations were made of the weighting functions of selected channels in the presence of hydrometeors for the tropical atmosphere case. Figures 3-15 and 3-16 show the weighting functions for the two lower frequency channels, for both sets of oxygen channels, in the presence of a nonprecipitating cloud of the same cloud liquid water density but at two different cloud depths. In the first instance (Figure 3-15), a uniform cloud of 0.6 g m^{-3} density was inserted into the atmosphere between the surface and 4 km. In the second instance (Figure 3-16), a similar cloud having the same density and base was used but the cloud extended to 8 km.
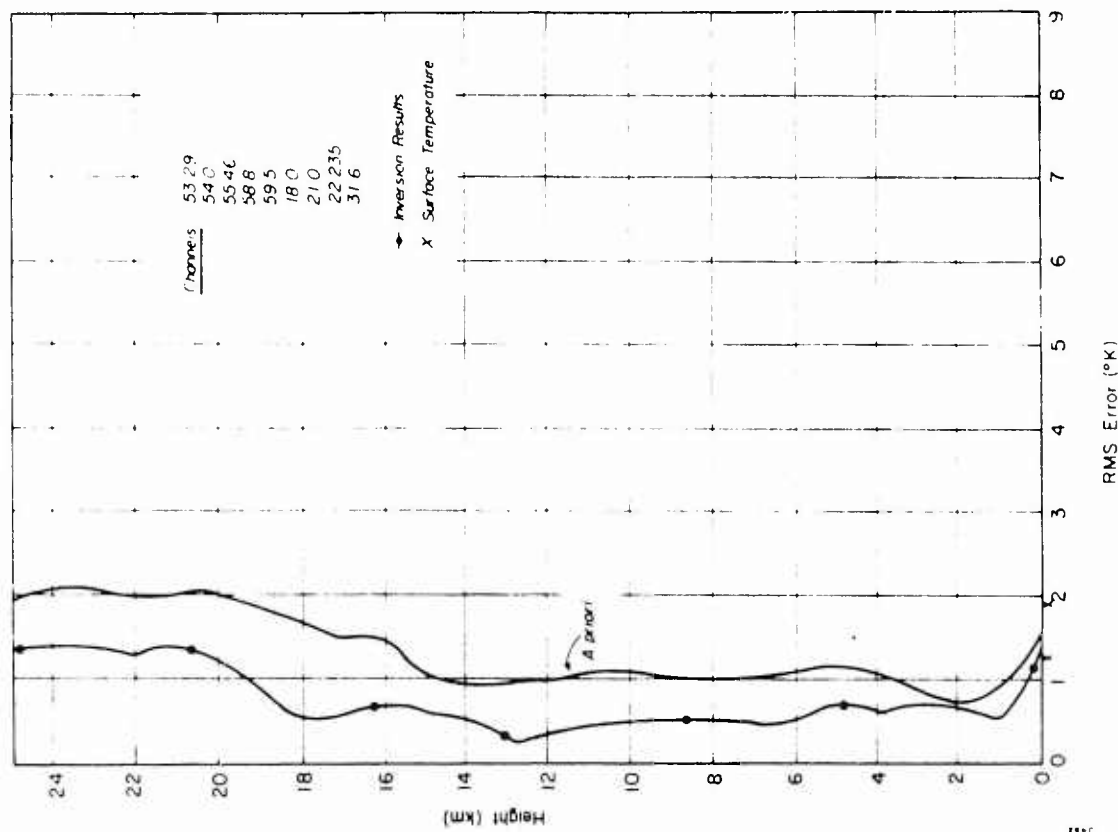
a) Temperature Inversion Results
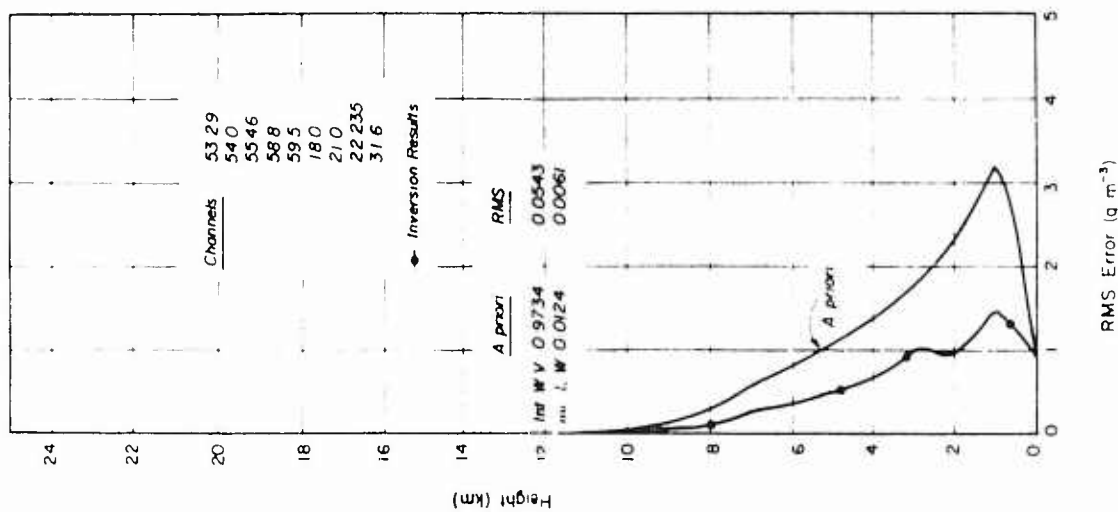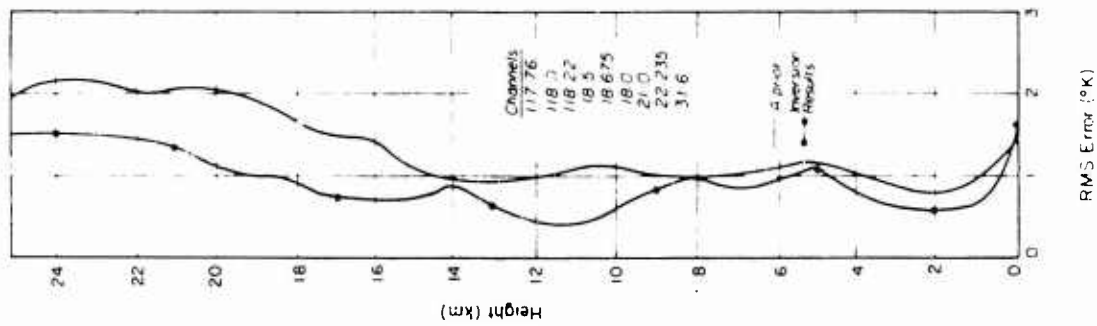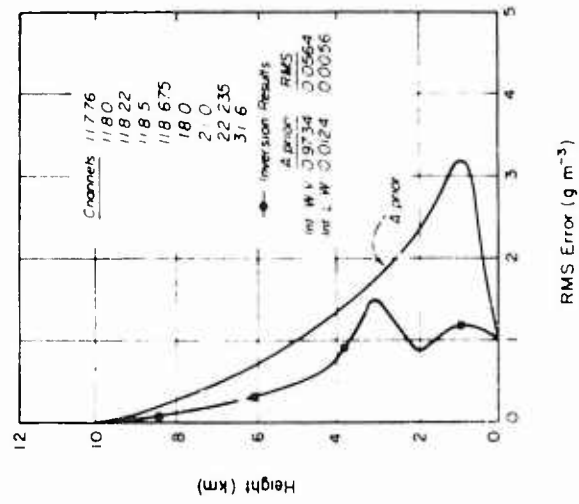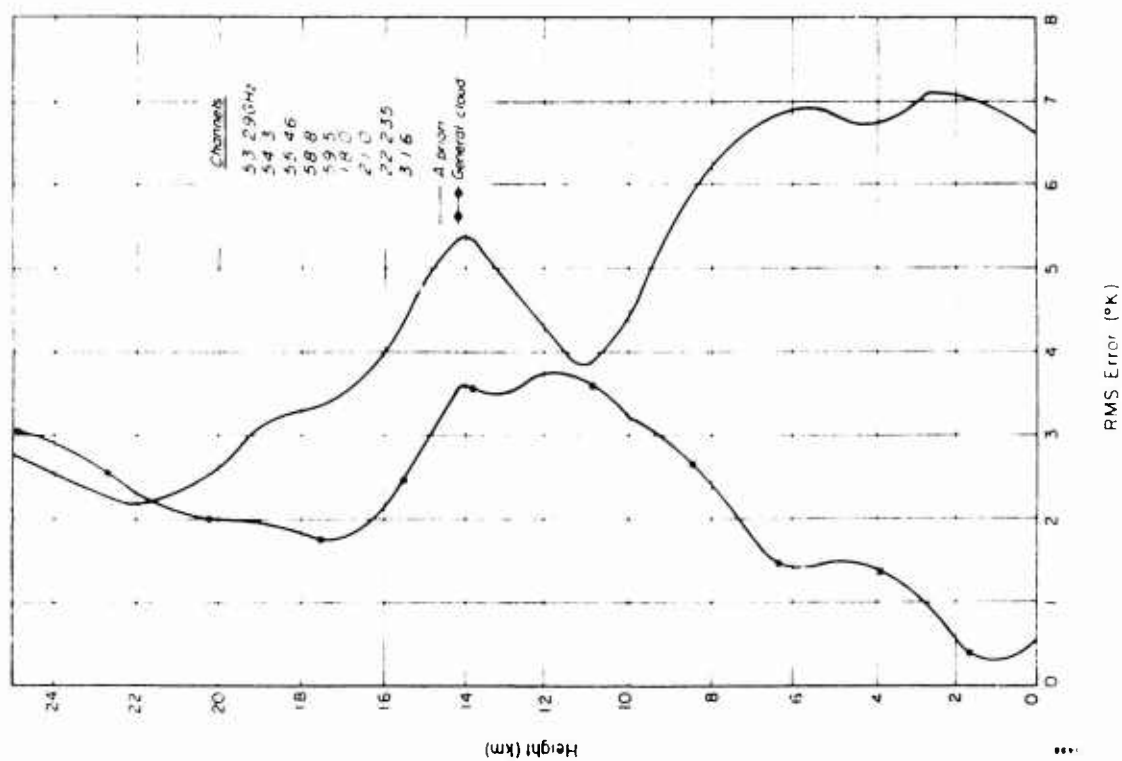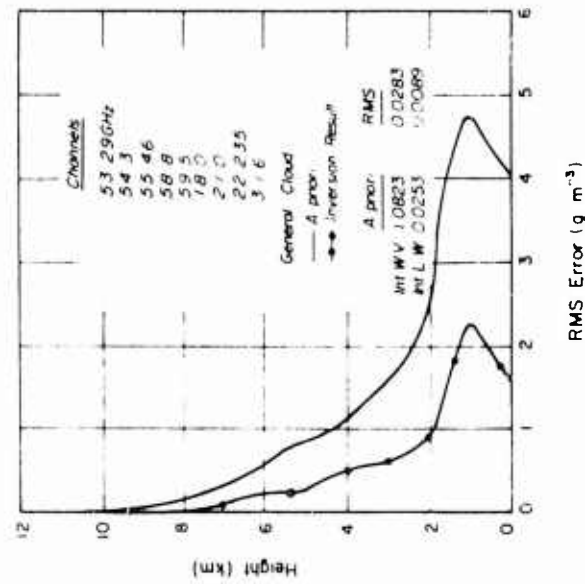
b) Water Vapor Density Inversion Results, and Integrated Liquid Water Content and Water Vapor (g cm⁻²)

Figure 5-15 Inversion Results for the Upward Looking Case Through the Midlatitude Atmosphere Using Channels in the 60 GHz Complex
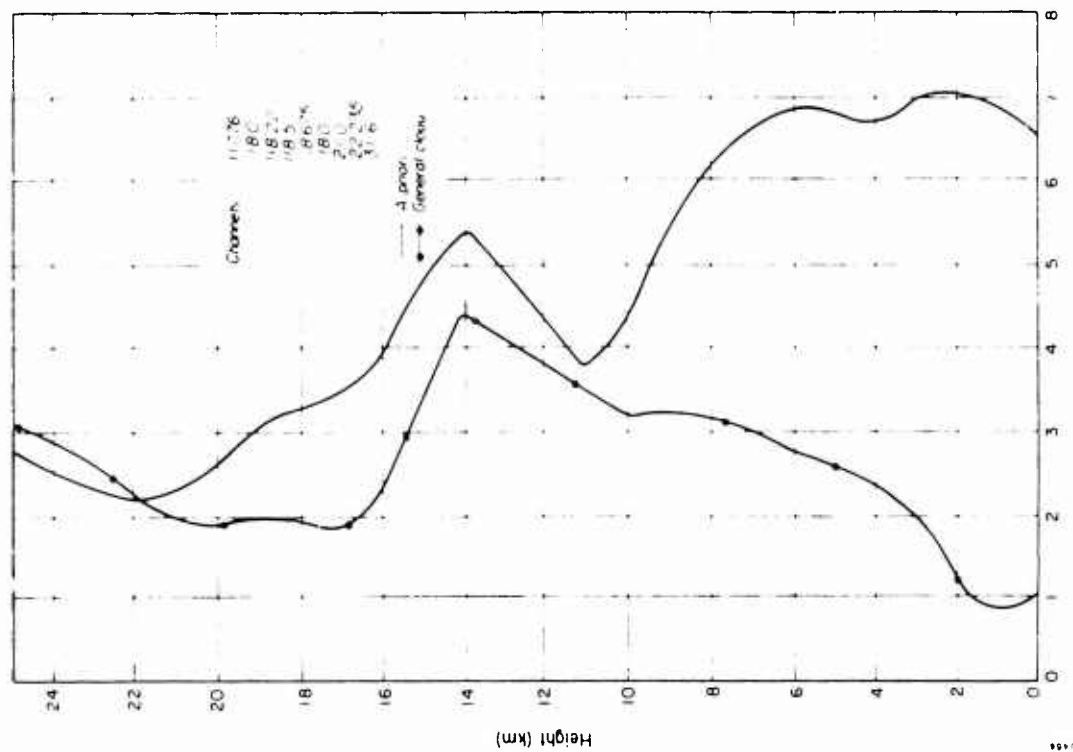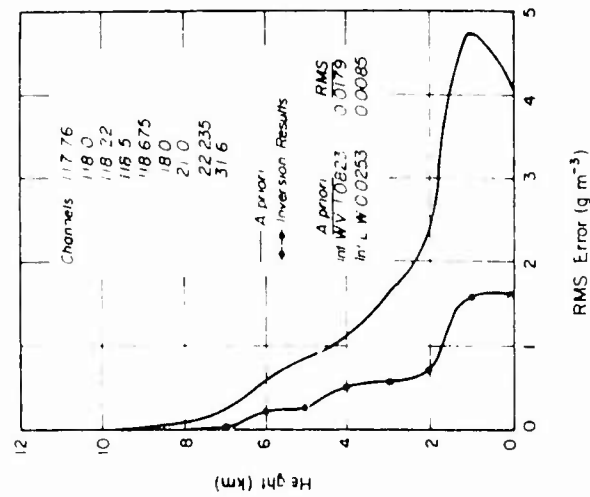
a) Temperature Inversion Results

b) Water Vapor Density Inversion Results, and Integrated Liquid Water Content and Water Vapor (g cm⁻²)

Figure 5-11 Inversion Results for the Upward Looking Case Through the Midlatitude Atmosphere Using Channels near the 1.35 cm Line
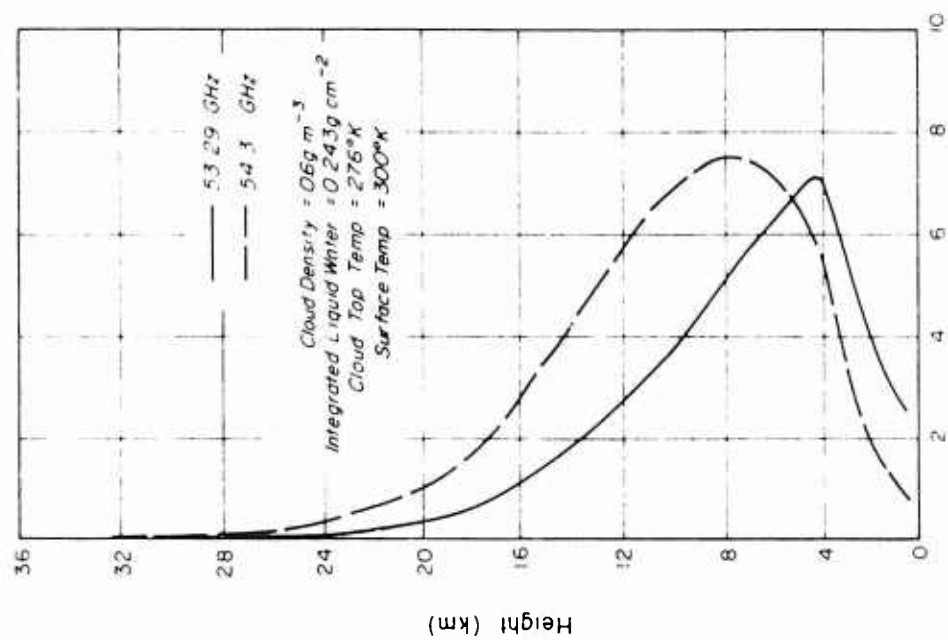
39

Temperature Weighting Function (Neper/m) × 10⁻⁵

b) The Two Lowest Frequency Channels near the 118 GHz Line

Temperature Weighting Function (Neper/m) × 10⁻⁵

a) The Two Lowest Frequency Channels in the 60 GHz Line

Figure 3-15 Temperature Weighting Functions of the Low Altitude Channels in the Presence of a 4 km Cloud

40

a) The Two Lowest Channels in the 60 GHz Complex

b) The Two Lowest Frequency Channels near the 118 GHz Line

Figure 3-16 Temperature Weighting Functions of the Low Altitude Channels in the Presence of an 8 km Cloud

41

The presence of these clouds, even in the case of the 4 km cloud, is clearly reflected in the 117.76 and 118.0 channels where the attenuation due to liquid water and the associated water vapor limits cloud penetration to one kilometer. Much less of an effect is seen in the lower frequencies, although the 8 km cloud causes substantial changes in the weighting functions for the 53.29 and 54.3 GHz channels, respectively. For the 4 km cloud the effect on the 53.29 GHz channel is clear; however, the 54.3 channel does not appear to be greatly influenced by this cloud.

The attenuation due to an ice layer above a cloud layer is shown in Figures 3-17 and 3-18 where an ice layer 2 km thick was added to the 4 km cloud, and a 4 km thick ice layer was added to the 8 km cloud. In comparing these figures with Figures 3-15 and 3-16, it is clear that the effect of ice on the oxygen channels is minimal, even for a 4 km ice layer.

The effects of precipitation on the weighting functions are shown in Figures 3-19 and 3-20. In these analyses the 4 km cloud has been replaced by a 4 km layer of uniform rain, and the 8 km cloud by 8 km of uniform rain capped by a 4 km layer of ice. The first case, that of the 4 km rain layer, is representative of tropical conditions with precipitation being initiated at the freezing level. The latter case is not meant to be realistic but is used simply as a limiting case for analysis. In comparing these two figures with those for the clouds of comparable thickness, the increased attenuation effects of precipitation are clearly evident. These effects are due to the enhanced effects of scattering as modeled in the precipitation approximation (see Section 2) and not to a difference in liquid water content. In fact, the liquid water content for the 4 km cloud exceeds that of the rain (0.24 g/cm^2 for the 4 km cloud vs. 0.12 g/cm^2 for the 4 km rain). The enhanced attenuation is much more dramatic for the lower frequency pair of channels since for the 4 km cloud case attenuation at 53.29 GHz was not significant. With precipitation the surface becomes obscured to all four channels.

These results also clearly demonstrate the frequency dependence of the differences between the ERT precipitation model and the Staelin approximation for clouds. As shown previously in Figure 2-5, the difference between the two approximations is near maximum at 50 GHz. The differences in weighting function at this frequency range should be large between

42

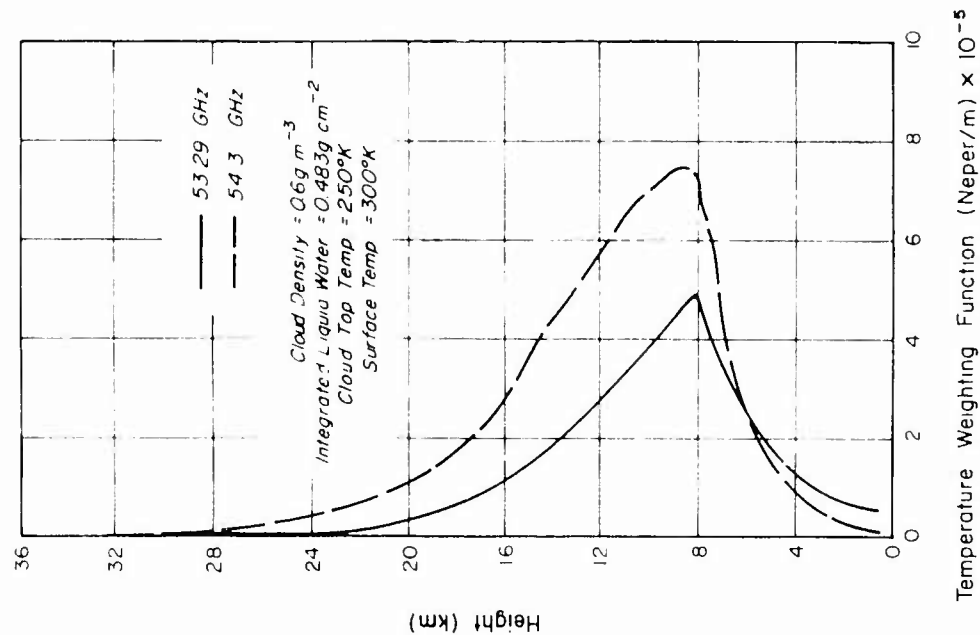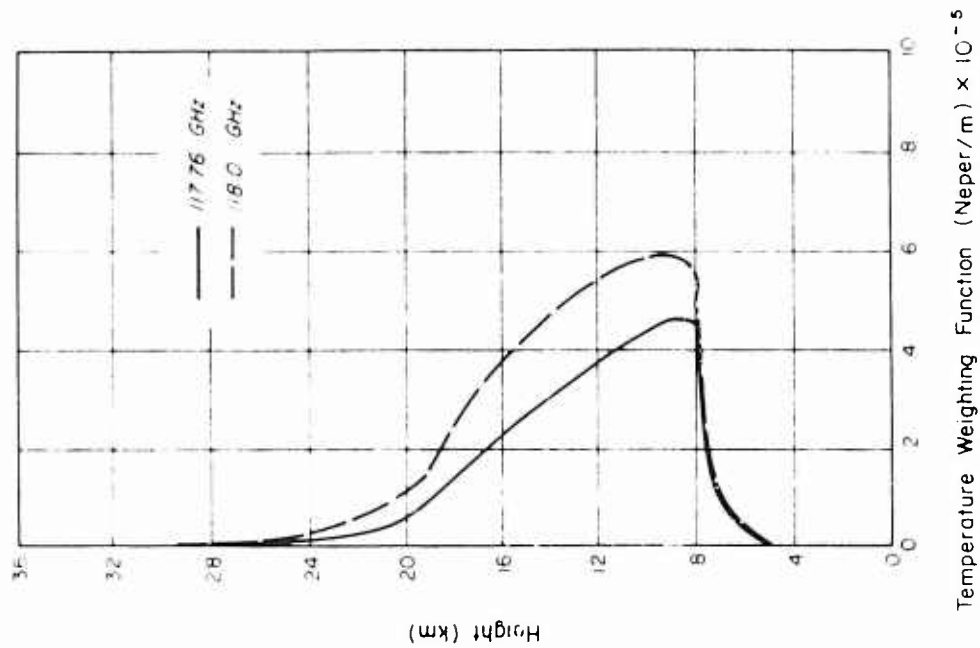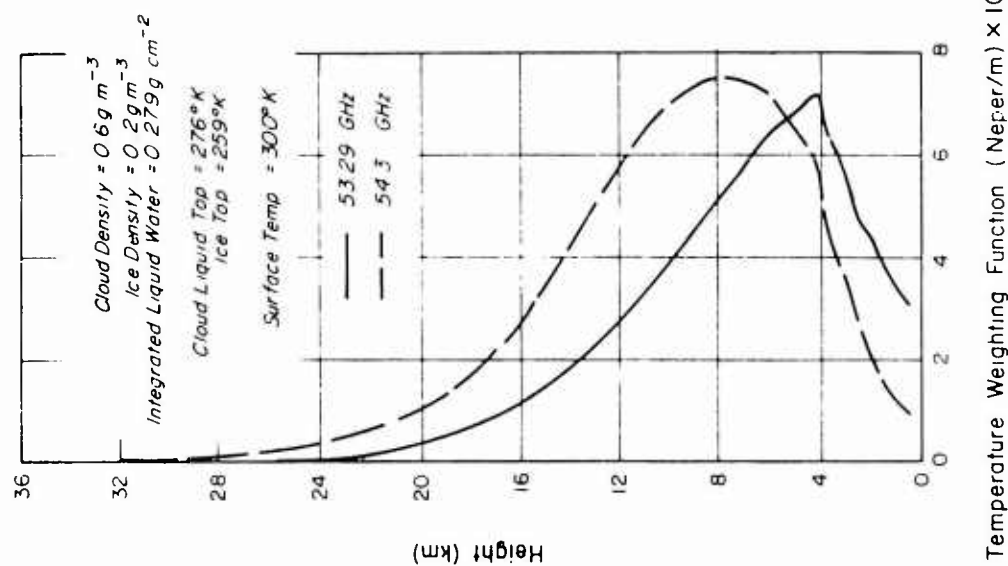Temperature Weighting Function (Neper/m) × 10⁻⁵

b) The Two Lowest Frequency Channels near the 118 GHz Line
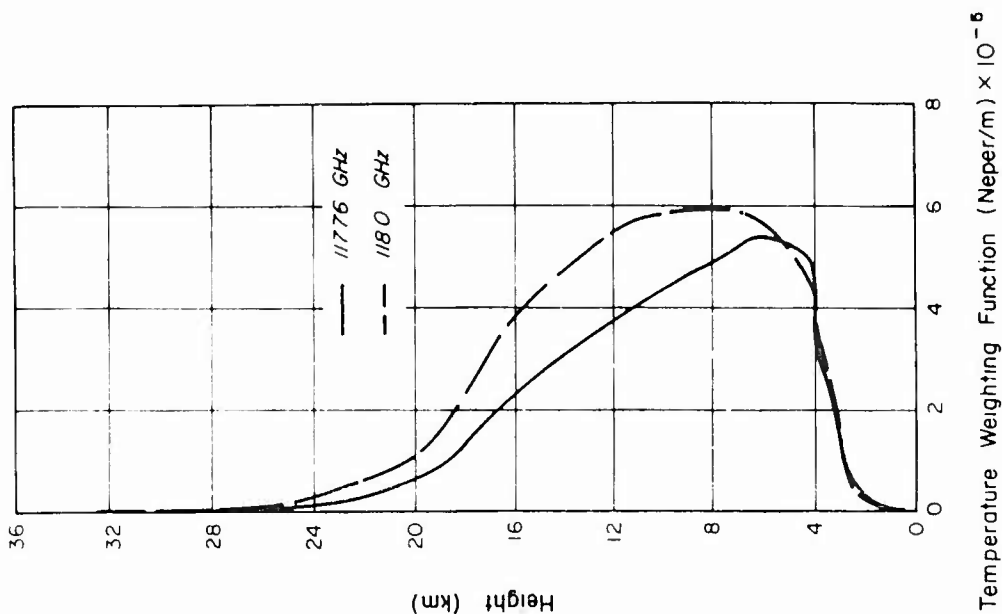
a) The Two Lowest Frequency Channels in the 60 GHz Complex

Figure 3-17 Temperature Weighting Functions for the Low Altitude Channels in the Presence of a 4 km Cloud Capped by a 2 km Layer of Ice

43

Temperature Weighting Function (Neper/m) × 10⁻⁵

a) The Two Lowest Frequency Channels in the 60 GHz Complex

b) The Two Lowest Frequency Channels near the 118 GHz Line

Figure 5-18 Temperature Weighting Functions for the Low Altitude Channels in the Presence of an 8 km Cloud Capped by a 4 km Layer of Ice

54

a) The Two Lowest Frequency Channels in the 60 GHz Complex

b) The Two Lowest Frequency Channels in the Presence of a 4 km 118 GHz Line

Figure 3-19 Temperature Weighting Functions of the Low Altitude Channels in the Presence of a 4 km Layer of Rain
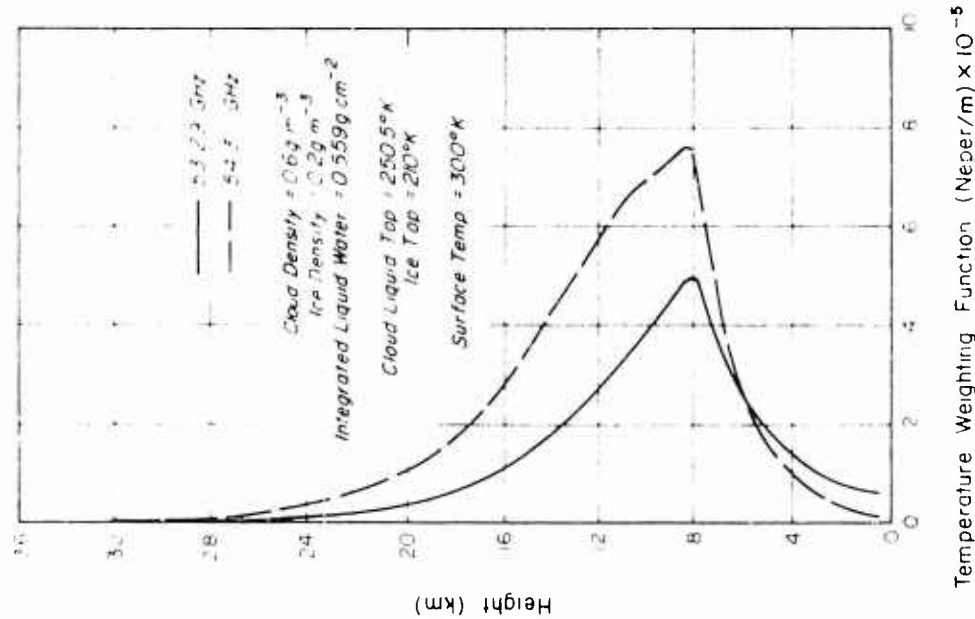
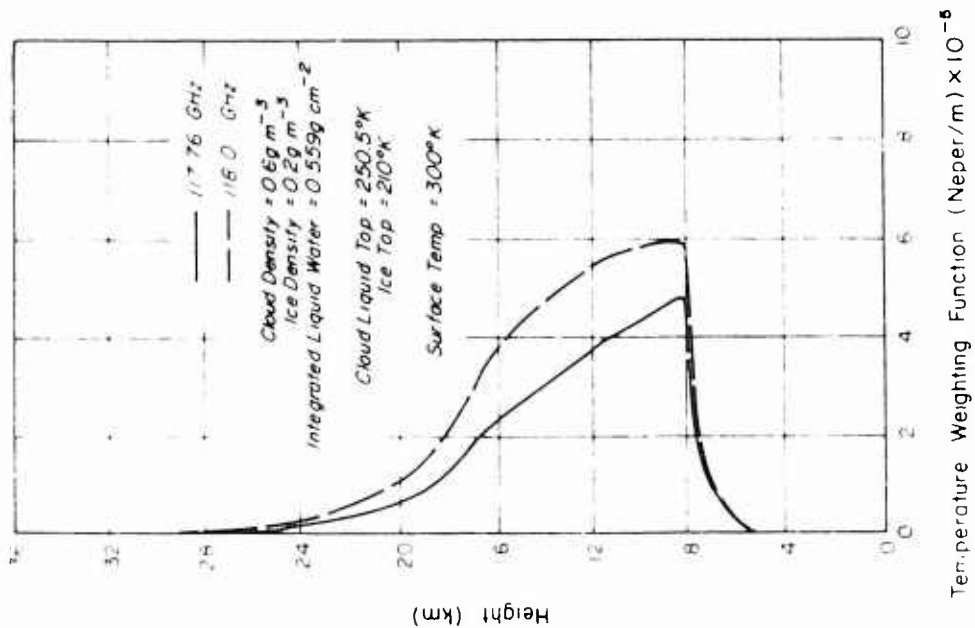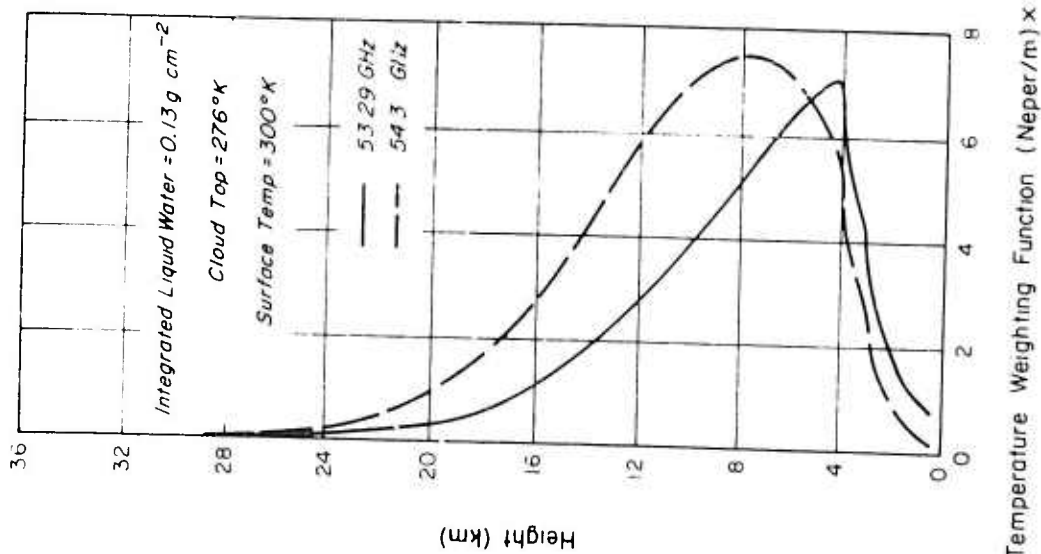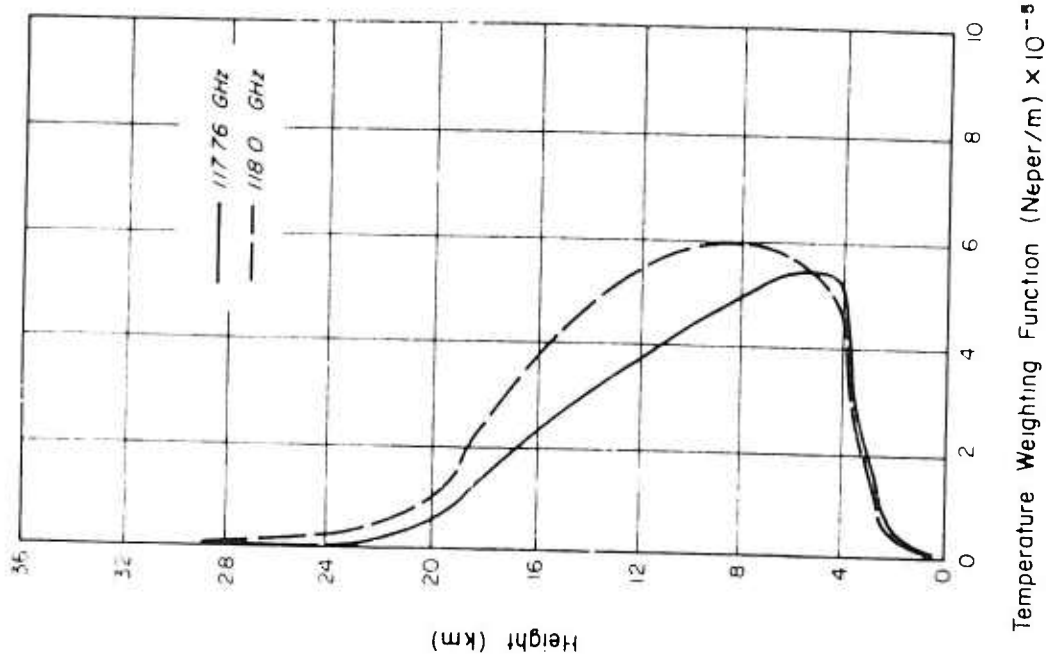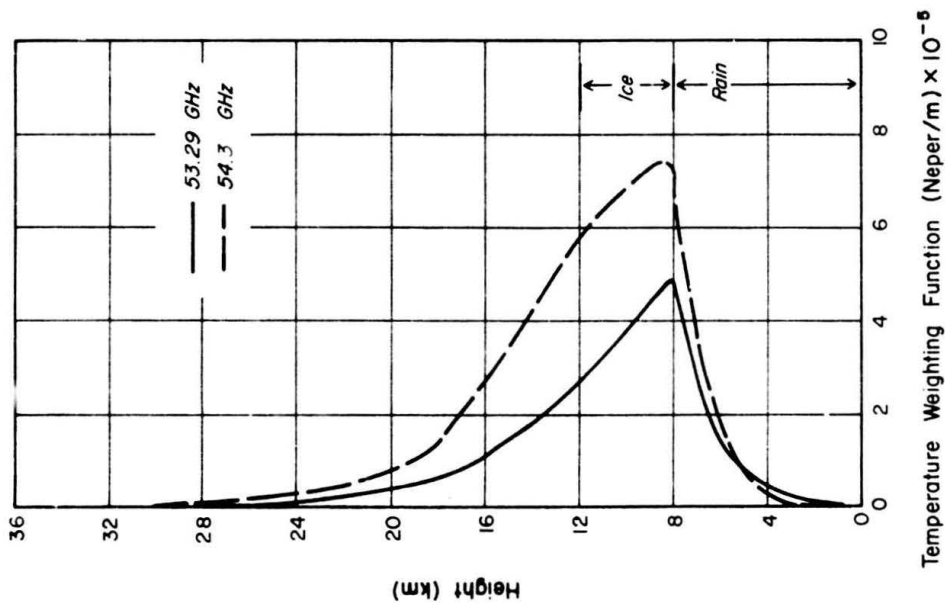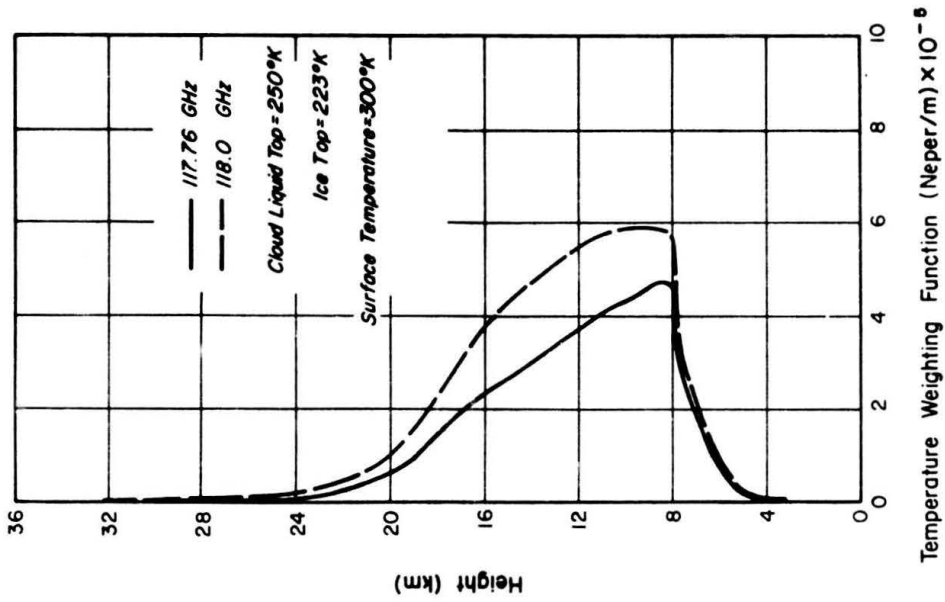a) The Two Lowest Frequency Channels in the 60 GHz Complex

b) The Two Lowest Frequency Channels near the 118 GHz Line

Figure 3-20 Temperature Weighting Functions for the Low Altitude Channels in the Presence of an 8 km Rain Layer Capped by a 4 km Ice Layer

those computed with cloud and the one computed with rain. At higher frequencies, the absorption coefficient computed by the two different approximations converges. Differences in the weighting function for clouds and for rain should therefore converge to zero at the higher frequencies, and appear to be doing so in the figures depicting the 118 GHz line.

The presence of an ice layer, even of 4 km thickness, does not appear to have any noticeable effect on the weighting functions.

Inversion analyses were systematically performed to evaluate, quantitatively, the effects of hydrometeors on temperature profiling. The results of these analyses are shown in Figures 3-21 and 3-22 for channels in the 60 GHz set, and in Figures 3-23 and 3-24 for the corresponding channels in the 118 GHz set. In each case the oxygen channels were used in conjunction with the water vapor and surface channels defined in Table 3-1. In every case the D-Matrix used for the inversion contained the distribution of clouds appropriate to the climatic regime.

Figure 3-21 shows the inversion results obtained for the 60 GHz channels, using an evaluation sample consisting of 36 clear-sky temperature profiles; the same temperature profiles, but with a uniform cloud of 2 km thickness and a density of 1 g/m^3; and the same temperature profiles but with a 2 km layer of rain having a uniform liquid water density of 1 g/m^3. The results are as one would expect from the analysis of the weighting functions. In the presence of clouds, the inversion errors increase over those for clear sky conditions. These errors are larger still for the rain case. In the atmospheric layer below 2 km the increase in rms error is over twofold in the presence of rain. The unexpected feature of these results is the fact that the increases in rms error are reflected at levels of the atmosphere significantly above the top of the hydrometeor layer. At 4 km, which is 2 km above the hydrometeor layer, the rms error for the precipitation case is over 1/2°K larger than for the corresponding clear-sky results. Significant, though unsystematic, differences in the rms results are evident even into the stratosphere. These differences are due to the fact that the lower channels do contribute signficicantly to the measurement of temperatures at the higher levels.

The effects of moving the cloud and rain layer to 4 km, in the case of the 60 GHz channels, are shown in Figure 3-22. Two significant effects can

47

Figure 3-22 Temperature Inversion Results Using the
60 GHz Channels for Elevated 2 km Cloud
and 2 km Rain Cases

Figure 3-21 Temperature Inversion Results Using the
60 GHz Channels for Clear Sky, 2 km Cloud,
and 2 km Rain Cases

48

Figure 5-24 Temperature Inversion Results Using the 118 GHz Channels for Elevated 2 km Cloud and 2 km Rain Cases
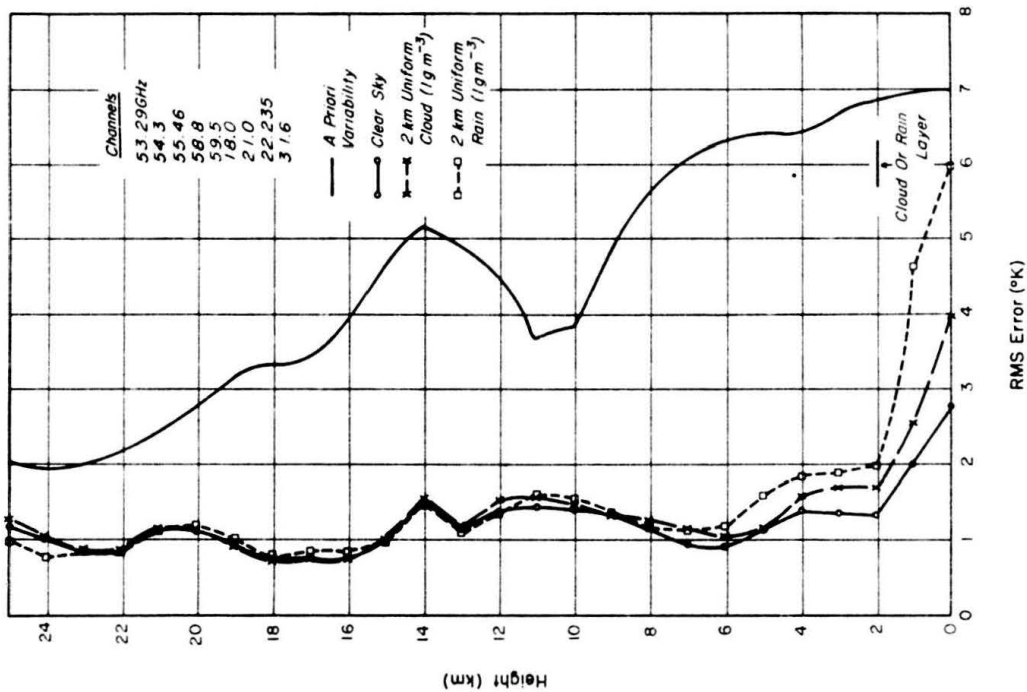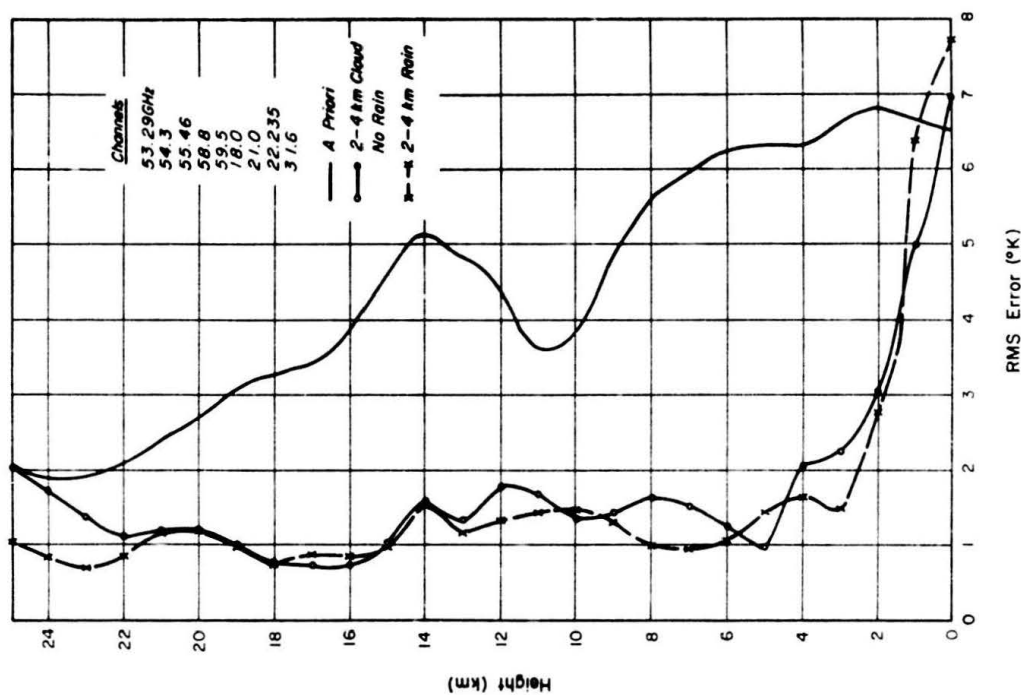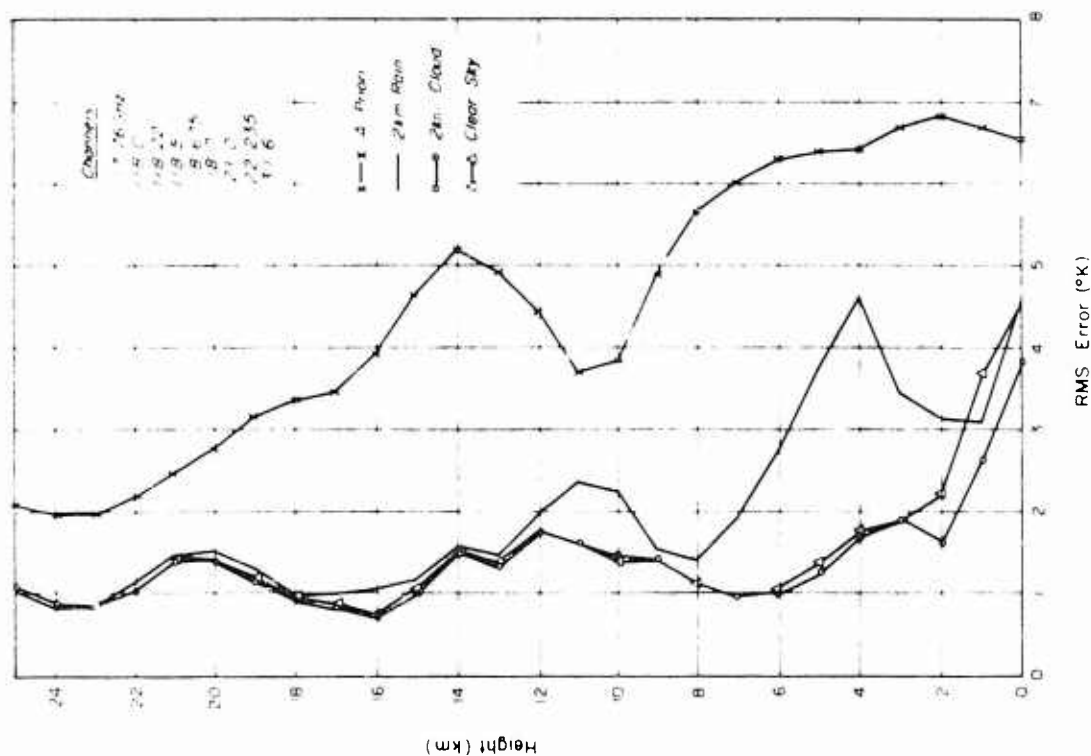
Figure 5-25 Temperature Inversion Results Using the 118 GHz Channels for Clear Sky, 2 km Cloud, and 2 km Rain Cases
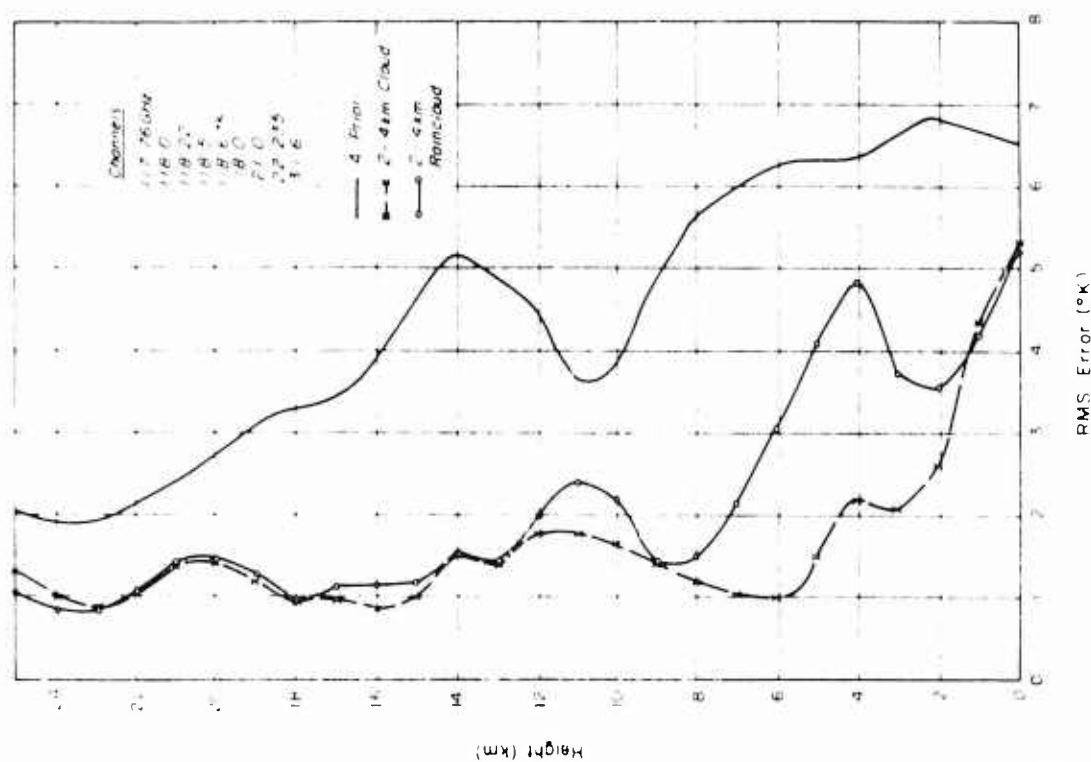
be noted. The inversion errors below the hydrometeor layer become totally unacceptable with rms errors in excess of 7°K at the surface, and 3°K at 2 km. The difference in rms error between the two cases is unsystematic and large. These results might be due to the fact that the data in the D-Matrix are unrepresentative of the conditions simulated by the evaluation samples. More likely, they indicate such severe attenuation in the lower channel, that all temperature information is lost below 4 km and the D-Matrix inversion is forced into unrealistic results.

The corresponding inversions for the 118 GHz channels are shown in Figures 3-23 and 3-24. These results show that there is a general increase in rms error with the hydrometeor layer elevated to 4 km. There are certain features which appear to be inconsistent with the results obtained for the 60 GHz channels. Better temperature inversion results can be obtained apparently with the 118 GHz channels for cloudy sky conditions that is possible for clear sky conditions.(Figure 3-23). However, it should be pointed out that due to the effect of water vapor absorption, very little information on temperature is really contained in these channels for levels of the atmosphere below 4 km. Figures 3-7 and 3-8 demonstrated that the lowest peak of this set of weighting functions in the presence of water vapor is at approximately 5 km, due to the wing of the 183 GHz water vapor line. Results obtained below this level are not reliable.

3.5 Effects of Droplet Size

Two models of hydrometeors were used in the inversion analysis presented in Section 3.4. The Staelin approximation was used to model the effects of clouds, while the ERT approximation was used to model precipitation effects. These approximation models were developed as an aid to the computation of the unit volume absorption by the hydrometeor particles. Their formulation is not appropriate for analysis of the effect of droplet size independent of the effects of absorption by the bulk liquid water content of the hydrometeors. As discussed in Section 2, the Staelin approximation for the Rayleigh regime provides a formulation of the unit volume absorption coefficient which is dependent only on the mass of water, and is independent of

50

any drop size parameter. The ERT approximation gives the unit volume absorption coefficient as an explicit function of the rainfall rate. Tracing through the derivations given in Section 2 of this approximation, it is possible to relate the volume absorption coefficient to a drop size parameter through the Marshall-Palmer distribution. However, it is not possible to decouple the drop size distribution and, therefore, a drop size parameter, from the bulk liquid water content of the hydrometeor. It is therefore impossible to perform an analysis of the effects of changing drop sizes with the bulk liquid water held constant using this model.

In order to satisfy the requirements for a realistic evaluation of the effects of drop size on brightness temperatures, computation was made using the full Mie approach and us ng the analytical distribution of Deirmendjian (1964). This distribution expresses the total number density function $N(r)$ explicitly in terms of the r iss density and a drop size parameter, the mode radius. The distribution i given by:

$$N(r) = A r^{C_1} \exp [-B r^{C_2}] \qquad 3\text{-}1$$

where

$$A = \frac{m C_2 B^{[\frac{C_1 + 4}{C_2}]}}{\frac{4}{3} \pi 10^6 r^{[-\frac{C_1 + 4}{C_2}]}} \qquad 3\text{-}2$$

and

$$B = \frac{C_1}{C_2 r_c^{C_2}} \qquad 3\text{-}3$$

where

    m is the mass density

    r_c is the mode radius

and

    C_1 & C_2 are two shape parameters

Computations were made of the brightness temperatures, through a tropical ocean atmosphere, using a hydrometeor layer with uniform mass density of 1 g/m^3 extending from the surface to 4 km. Three sets of computations were made, with mode radius at 20, 100 and 500 μm. A mode radius of 20 μm is representative of the spectrum for cloud droplets, and a mode radius of 500 μm is representative of rain. The 100 μm mode radius was selected to examine the transition between cloud and rain.

Results of the computations for the frequency range between 3 and 118 GHz are shown in Figure 3-25. As to be expected, all three curves converge. For the three droplet sizes used this occurs near 60 GHz. The convergence is due to the fact that as the drop size becomes large, relative to the wavelength, the Mie efficiency factor tends to be a limiting value of 2. The computations show that for realistic models of rain and cloud drop size distributions, no drop size dependence is expected for frequencies higher than 60 GHz.

The low end of the frequency spectrum shows the convergence of the curves for r_c = 20 μm and r_c = 100 μm. If the computations had been performed for frequencies lower than 3 GHz, the results would show a convergence of all three curves at some lower frequency. This convergence is predicted by the Staelin approximation which states that as the drop size becomes smaller, relative to wavelength, the unit volume absorption coefficient (and, therefore, the brightness temperature) are independent of drop size, but are a function of the water mass. Extrapolating the three curves to lower frequencies, an approximate convergence frequency of approximately 1 GHz can be obtained for the range of mode radii between 20 and 500 μm. Below 1 GHz, then, no drop size effect is expected.

If the range of mode radii between 20 and 100 μm is representative of limiting conditions for clouds, Figure 3-25 shows that a cloud drop size effect can be expected in the range of frequencies between 3 and 60 GHz, with the maximum effect at approximately 10 GHz. For raindrops in the range of 100 to 500 μm, significant drop size effects are found in the frequency range between 1 and 10 GHz, with maximum effects at approximately 3 GHz.
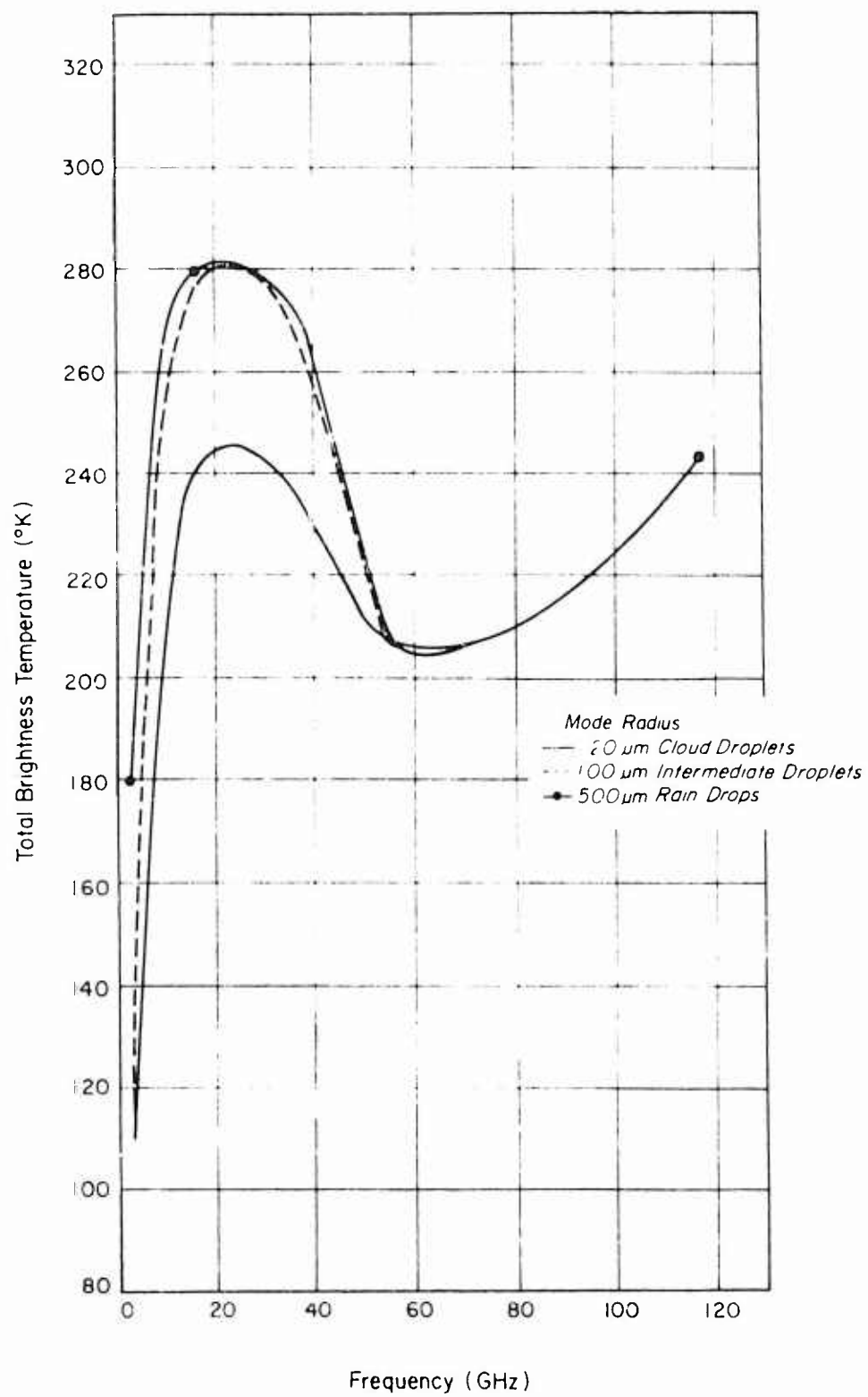
Figure 3-25 Dependency of Total Brightness Temperature on Cloud Drop Size and Frequency

4. PROBING FOR CLOUD PARAMETERS

4.1 Previous Results

In previous analyses of microwave techniques to probe cloud parameters, the focus has been on the use of the 22.235 GHz line of water vapor. Multichannel techniques, with channels on the wings of the line and at near-line center, were developed and analyzed as a means of separating out the effects of water vapor from those of the liquid water content of clouds. Typical of these studies is that by Gaut, Reifenstein and Chang (1972). Experimentally, the Nimbus E Microwave Spectrometer (NEMS), with channels at 22.235 and 31.40 GHz in addition to three oxygen channels, has demonstrated that it is possible to obtain integrated cloud liquid water and integrated water vapor from these techniques.

However, very little work has been done to extend these techniques to obtain additional parameters with regard to clouds. Of immediate interest to the Air Force, for example, is the possibility of discrimination between glaciated and unglaciated clouds, and in the case of glaciated clouds the height of the water cloud top as well as the height of the entire cloud. It would also be of interest to be able to profile the vertical distribution of liquid water to better define the layering structure of the clouds.

A study was undertaken to extend the analysis of remote cloud probing by microwave techniques to include these parameters. Furthermore, the analysis, in terms of frequency, was extended to include the 183 GHz water vapor line. The simultaneous use of an infrared channel in cloud probing was also examined. The results of this study are presented in this section.

4.2 Liquid Water Profile

The study of liquid water vapor profiling was very preliminary. The analysis focused on the ability of microwave remote sensors to provide integrated cloud liquid water in a number of thick layers in the atmosphere. As a test, the atmosphere was divided into only three layers as shown in the table that follows.

Preceding page blank

Layer	Altitude Range	Cloud Regime
1	Surface to 3 km	Low clouds
2	3 km - 6 km	Middle clouds
3	6 km - 20 km	High clouds

Inversion analysis was then performed with various combinations of channels. The results of this analysis are shown in Table 4-1

The atmospheric regime selected for the inversion analysis was that representative of midlatitude spring. The sample size of the data used to generate the D-Matrix was 84 and the evaluation sample size was 36. Five sets of channels were analyzed, as shown below.

First Case - Channels located only in the 60 to 118 GHz oxygen complexes.

Second and Third Cases - Oxygen channels in combination with one water channel

Fourth Case - Oxygen channels in combination with two water channels

Fifth Case - Channels which included no oxygen channels

In examining the results, it is interesting to note that independent of the channel combinations, the best results in terms of the figure of merit are obtained for the liquid water in the lowest layer. This is the layer with the largest variability in liquid water (a priori rms variability of 0.026 g/cm^2). It is encouraging that with microwave measurements the rms error in the inferred values for this layer is significantly better than climatology. The best overall results, for all three layers, are obtained when the two sets of oxygen channels are used in conjunction with the two water vapor channels at 183 and 22 GHz, respectively. The fact that acceptable results are obtainable with the oxygen channels alone (First Case)

TABLE 4-1

INVERSION RESULTS FOR INTEGRATED WATER VAPOR AND LAYER INTEGRATED LIQUID WATER

Atmospheric Region: <u>Midlatitude Spring</u>

D-Matrix Sample Size: $\frac{84}{36}$
Evaluation Sample Size: $\frac{84}{36}$

Parameters (g/cm^2)	A Priori	A and B		A and B + 22		A and B + 183		A and B, 183 and 22		57,94,140,170 and 183	
		Std. Dev.	Figure of Merit	Std. Dev.	Figure of Merit	Std. Dev.	Figure of Merit	Std. Dev.	Figure of Merit	Std. Dev.	Figure of Merit
Integ. Water Vapor	1.0823	0.4955	2.184	0.0513	21.079	0.3795	2.852	0.0462	23.421	0.6612	1.637
Layer 1: Liquid Water	0.0260	0.0149	1.740	0.0090	2.889	0.0097	2.678	0.0070	3.691	0.0108	2.412
Layer 2: Liquid Water	0.0048	0.0037	1.280	0.0034	1.404	0.0036	1.341	0.0032	1.476	0.0038	1.263
Layer 3: Liquid Water	0.0056	0.0041	1.380	0.0036	1.552	0.0037	1.496	0.0035	1.580	0.0042	1.322

Channels (GHz)

A: 53.29 GHz   B: 117.76 GHz   Layer 1: 0 to 3 km
   54.30   118.00   Layer 2: 3 to 6 km
   55.46   118.22   Layer 3: 6 to 20 km
   58.80   118.5
   59.50   118.6-5

is probably due to the effects of the 183 GHz water vapor line extending into the 118 GHz region. The overall results suggest that it is possible to obtain, in a gross sense, the layering structure of cloud fields from microwave remote sensing.

4.3 Cloud-Type Discrimination and Cloud Top Altitude Determination

The approach to this analysis was to assume that an infrared channel, similar to the window channel on the DMSP, coincidently views a cloud with the microwave radiometer. Furthermore, it is assumed that the clouds are optically thick and of sufficient horizontal extent such that the effective blackbody temperature, T_{bb}, measured by the infrared channel, approximates for all practical purposes the actual physical temperature of the air at equilibrium with the cloud top. This cloud top temperature would correspond to the temperature of the physical top of the cloud, regardless of the phase characteristics of the cloud top layer. If a microwave frequency is found such that it is totally transparent to ice, but highly opaque to liquid water, its brightness temperature would be well correlated with the top of the liquid portion of the cloud. The difference between the effective blackbody temperature measured by the IR channel and the brightness temperature measured by this microwave channel would provide information on the presence of a glaciated layer. Furthermore, the measured temperatures themselves would provide data on the heights of the water cloud top and the ice cloud top.

Analysis was performed to find a suitable microwave channel to work with the infrared channel. The analysis focused on the use of the 183 GHz water vapor line which is much more opaque than the 22 GHz line. Furthermore computations shown in Figure 3-25 demonstrate that at the higher frequencies the brightness temperature for a hydrometeor layer is independent of drop size. Computations were made for three frequencies at 140 and 170 GHz on the wings of the line and at 183 GHz near line center. For the sake of analysis, three cloud model conditions were assumed: a 4 km cloud layer extending to the surface, the same cloud layer but with a 2 km layer of ice above it, and an 8 km water cloud with a 4 km layer of ice. The temperatures of the cloud tops for these models are summarized in Table 4-2.

TABLE 4-2

SUMMARY OF THE TEMPERATURE CHARACTERISTICS OF CLOUD MODELS
USED FOR ANALYSIS

Cloud Model	Temperature (K)		Assumed Infrared
	Liquid	Ice	
4 km water	275.6	NA	275.6
4 km and 2 km ice	275.6	263.7	263.7
8 km water and 4 km ice	250.0	223.3	223.3

Results of these computations are shown in Figures 4-1a and 4-1b. Figure 4-1a shows that the brightness temperature at the selected frequencies are only weakly dependent on cloud liquid water content. Furthermore, the brightness temperature at 170 GHz is almost identical to the physical temperature of the cloud top. Similar computations for an 8 km liquid water cloud, with cloud top at 250°K, also showed that the brightness temperature at 170 GHz corresponds quite well to the physical temperature of the cloud top. Further analysis is required to demonstrate whether or not this correspondence holds in the general case.

The effects of an ice layer on IR effective temperature and microwave brightness temperature is shown in Figure 4-1b. For these calculations, the liquid cloud properties were held constant with a liquid cloud density of 0.6 gm/cm^3 (corresponding to an integrated liquid water content of 0.25 gm/cm^2 for the 4 km cloud layer). The ice density in the 2 km ice layer was changed; thus effectively changing the equivalent liquid water content of the ice layer without changing the geometric properties of the cloud. The plotted IR effective cloud top temperature again assumed that the ice layer is essentially opaque in the IR; thus the effective blackbody temperature measured in the IR corresponds to the geometric top of the entire cloud.

In comparing the results shown in the two figures, it is seen that within the limits of the models used in the calculations, the microwave brightness temperature of clouds at these selected frequencies are not strongly dependent on the density of an ice layer. These results imply that brightness temperatures obtained using channels at these high

frequencies, when used with concurrent IR blackbody temperatures, can be of use to:

a) differentiate between glaciated from unglaciated clouds, and

b) estimate the height of both the top of the cloud and the top of the liquid cloud in the presence of an ice layer.

Computations using an 8 km water cloud with and without a 4 km ice layer support the results shown here for the 4 km cloud case. Further research, however, is needed to pinpoint a useful operational technique applicable to clouds with much more complex structure than those modelled in this study.
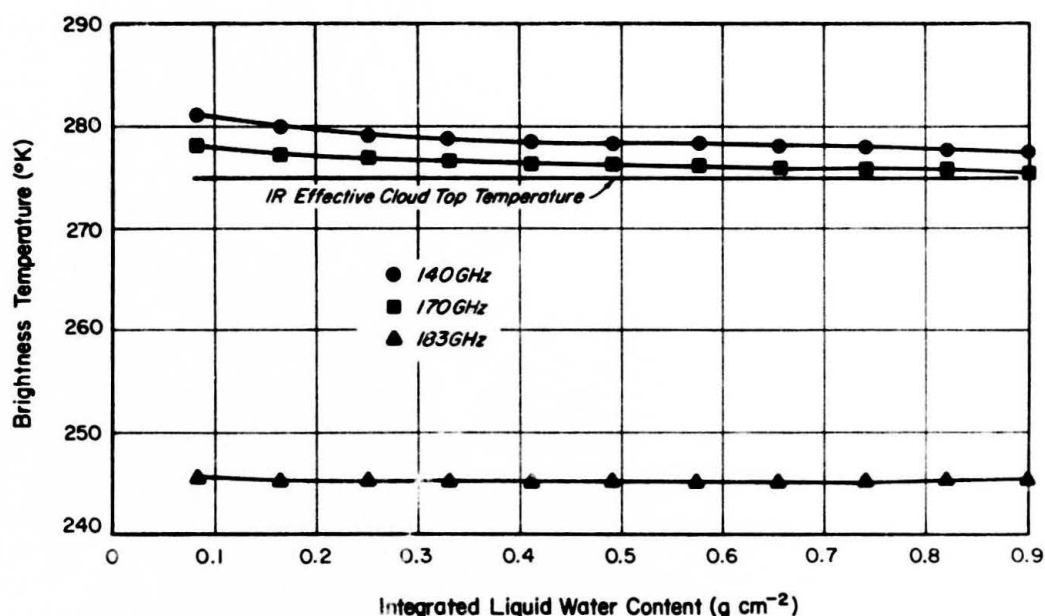
a) Liquid Clouds with Cloud Top Temperature
    at 275.6° K
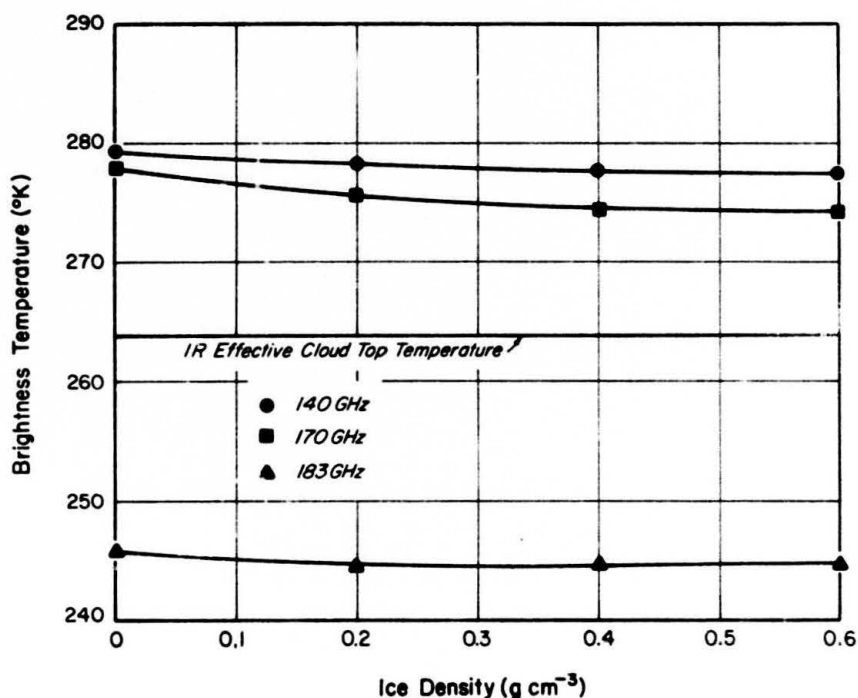
b) Glaciated Clouds with Liquid Cloud Top
    Temperature at 275.6°K and Ice Cloud
    Top Temperature at 263.7°K

Figure 4-1   Microwave and Infrared Measurements of Glaciated and Unglaciated Clouds

5. SUMMARY AND CONCLUSIONS

An approximate model for the computation of the unit extinction coefficient for rain has been developed to facilitate simulation and inversion analyses. In terms of the interaction, the model assumes that the efficiency factor as a function of drop radius can be approximated by three regimes: Rayleigh expression, transition, and large sphere. Analytical expressions have been developed for these regions such that the convolution of the efficiency factor with the Marshall-Palmer distribution, by which the drop size distribution is expressed, can be integrated in closed form. The use of the Marshall-Palmer distribution, taken from meteorological radar studies, results in an expression which relates the synoptic parameter rainfall rate to the precipitation extinction in a given layer. In addition, temperature dependence and wavelength dependence are analytically expressed providing a realistic layer parameterization which is amenable to numerical computation. It has been shown that the computed extinction coefficients faithfully reproduce full Mie computations within a reasonable accuracy. This development enables computations of the extinction effect of precipitation in atmospheres with realistic temperature structure without resorting to the full Mie expansion.

This model for rain, and the Staelin model for clouds, were used to investigate the effects of hydrometeors on temperature inversion accuracies. The inversion algorithm used was the statistical method, and it was applied to two sets of channels: one in the 60 GHz complex and the other in the 118 GHz complex of oxygen. In general, the results show that clouds and rain do have significant deteriorating effects on temperature inversion accuracies. These effects are much more pronounced in the case of the channels in the 118 GHz region. Furthermore, the hydrometeors tend to produce errors in inversion at altitudes many kilometers above the tops of the layers.

The effects of drop size on the brightness temperature of hydrometeor layers were separately analyzed using the full Mie expansion and the Diermendjian expression for drop size distribution. For the model cloud analyzed, the results indicate that the effect of drop size on brightness temperature is separable into two regimes: rain and clouds. For rain, the effects of drop size are confined to the frequency range between 1 and 10 GHz, with maximum effects at 3 GHz. For cloud droplets, the effects of drop size can be noted in the range of frequencies from 3 to 60 GHz, with

maximum effect at 10 GHz. It would appear that the frequency region best suited for remote probing of drop size parameters is found between 3 and 10 GHz, provided that some independent measurements can be made to separate out the effects of bulk liquid water of the hydrometeors.

Inversion analysis performed in this study suggests that with the right combination of channels, it is possible to infer the layered structure of clouds. Furthermore, by using a very opaque channel located in the wing of the 183 GHz water vapor line in conjunction with an infrared channel, the possibility to differentiate glaciated clouds from water clouds exists. The same channels can provide additional information about the height of the top of the liquid cloud as well as that of the ice layer.

6. REFERENCES

Debye, P., 1929: _Polar Molecules_, Dover Press.

Deirmendjian, D., 1964: "Scattering and Polarization Properties of Water Clouds and Hazes in the Visible and Infrared," _Appl. Optics_, Vol. 3.

Gaut, N. E. and E. C. Reifenstein, III, 1970: _Interaction of Microwave Energy Within the Atmosphere_, paper presented at AIAA Earth Resources Observations and Information Systems, Annapolis, Maryland, ERT Technical Report No. 10.

Gaut, N. E., E. C. Reifenstein, III and D. T. Chang, 1972: _Microwave Properties of the Atmosphere, Clouds and the Oceans_, Final Report. Contract No. NAS 5-21194, Environmental Research & Technology, Inc.

Gaut, N. E., E. C. Reifenstein, III, D. T. Chang and J. C. Blinn, III, 1973: _Analysis of Microwave Sounding Systems_, Final Report. ERT No. P-553, Environmental Research & Technology, Inc.

Grant, E. H., T. J. Buchanan and H. F. Cook, 1957: "Dielectric Behavior of Water and Microwave Frequencies," _J. Chem. Phys._, Vol. 26.

Gross, E. P., 1955: "Shape of Collision-Broadening Spectral Lines," _Physical Review_, Vol. 97.

Lorentz, M. A., 1952: _The Theory of Electrons and Its Applications to the Phenomena of Light and Radiant Heat_, Dover Press.

Marshall, J. S. and W. M. Palmer, 1948: "The Distribution of Raindrops with Size," _J. Meteor._, Vol. 5.

Meeks, M. L. and A. E. Lilley, 1963: "The Microwave Spectrum of Oxygen in the Earth's Atmosphere," _J. of Geophys. Res._, Vol. 68.

Mie, G., 1908: _Ann. Phys._, Vol. 25.

Reber, E. E., 1972: "Absorption of the 4- to 6-Millimeter Wavelength Band in the Atmosphere," _J. of Geophys. Res._, Vol. 77.

Shifrin, K. S. and M. M. Chernyak, 1968: "Absorption and Scattering of Microwaves in Precipitation," in _Transfer of Microwave Radiation in the Atmosphere_, K. S. Shifrin (ed), NASA TT F-590.

Staelin, D. H., 1966: "Measurements and Interpretations of the Microwave Spectrum of the Terrestrial Atmosphere Near 1-Centimeter Wavelength," _J. of Geophys. Res._, Vol. 71.

Westwater, E. R., 1972: "Microwave Emission from Clouds," NOAA Technical Report ERL 219-WPL 18.

Van Vleck, J. H. and V. F. Weisskopf, 1945: "On the Shape of Collision Broadened Lines," Rev. Mod. Phys., Vol. 17.

Wexler, R. and D. Atlas, 1963: "Radar Reflectivity and Attenuation of Rain," J. App. Met., Vol. 2.